Convection under rotation for Prandtl numbers near 1: Linear stability, wave-number selection, and pattern dynamics

Yuchou Hu,[1,2] Robert E. Ecke,[1] and Guenter Ahlers[2]
[1]*Condensed-Matter and Thermal Physics Group, Center for Nonlinear Studies, Los Alamos National Laboratory, Los Alamos, New Mexico 87545*
[2]*Department of Physics and Center for Nonlinear Sciences, University of California, Santa Barbara, California 93106*
(Received 4 December 1996)

Rayleigh-Bénard convection with rotation about a vertical axis was studied with the shadowgraph imaging method up to a dimensionless rotation rate Ω of 22. Most of the results are for a cylindrical convection cell with a radius-to-height ratio $\Gamma=40$ that contained CO_2 at 33.1 bars with a Prandtl number $\sigma=0.93$. Measurements of the critical Rayleigh number R_c and wave number k_c for $0<\Omega<22$ agree well with predictions based on linear stability analysis. Above onset and with rotation, the average wave number and details of the pattern dynamics were studied. For $\Omega\lesssim 5$, the initial onset was to a pattern of straight or slightly curved rolls. For $0.1\lesssim\epsilon\equiv\Delta T/\Delta T_c-1\lesssim 0.5$ but below the onset of spiral-defect chaos, rotation with $\Omega\lesssim 8$ produced weak perturbations of nonrotating patterns. Typically, this gave an ''S-shaped'' distortion of the zero-rotation pattern of straight or somewhat curved rolls. Rotation had a stronger effect on the source and motions of dislocation defects. For $\Omega>0$ the defects were generated primarily at the wall, whereas for $\Omega=0$ they were nucleated in the bulk via the skewed-varicose instability. Rotation picked a preferred direction of motion for the defects once they formed. For $\epsilon\gtrsim 0.5$, recognizable spiral-defect chaos and the oscillatory instability were observed for $\Omega\lesssim 12$. For $\Omega\gtrsim 8$, domain growth and front propagation suggestive of the Küppers-Lortz instability were observed from onset up to an ϵ value that increased with Ω. Increasing ϵ at fixed $\Omega\lesssim 12$ enhanced dislocation-defect dynamics over Küppers-Lortz front propagation. Quantitative measurements of average pattern wave numbers, correlation lengths, and spatially averaged roll curvature as functions of ϵ and Ω are presented. At a fixed $\Omega\gtrsim 10$, the average wave number had two distinct wave-number-selection regions with different slopes as a function of ϵ, one above $\epsilon\approx 0.45$ and the other near onset. The slope for ϵ near onset reached a minimum at $\Omega=12.1$ and increased linearly for $12<\Omega<20$. [S1063-651X(97)03906-8]

PACS number(s): 47.20.Bp, 47.54.+r, 47.32.−y

I. INTRODUCTION

Rayleigh-Bénard convection with rotation is a simple laboratory system incorporating essential forces that occur in natural phenomena such as circulations in the atmosphere and ocean currents. It provides an ideal setting for the study of the interaction between thermally induced instabilities and Coriolis and centrifugal forces arising from rotation. Theoretical analysis [1–4] of the problem has concentrated on the limit where the centrifugal force is much less important than gravity and can be neglected. Experimentally this limit can be well approximated by a combination of suitable physical rotation frequencies f, lateral system size L, and sample thickness d for which the centrifugal acceleration $(2\pi f)^2 L$ is much smaller than the gravitational acceleration g. Under the same conditions, the relevant dimensionless frequency

$$\Omega\equiv 2\pi f d^2/\nu, \tag{1}$$

which measures the strength of the Coriolis force, can cover a wide range of interest (ν is the kinematic viscosity). The simple geometry of the problem, a thin horizontal layer of fluid, combined with the easily controlled parameters of heating from below and rotation about a vertical axis, makes this system experimentally attractive. Despite these features, relatively little experimental work has been done on this system in the region close to the onset of convection. Most of the previous work [5–18] was qualitative or semiquantitative, sparse in covering parameter space, well above onset, or without good flow visualization.

Linear stability analysis [1] predicts that convective motion in the form of rolls appears in the fluid when the temperature difference ΔT across the layer exceeds a critical value ΔT_c that depends on the rotation rate. The dimensionless distance from the onset of convection is measured by $\epsilon\equiv\Delta T/\Delta T_c(\Omega)-1$. Rotation inhibits the onset of convection and decreases the wavelength λ of the convection rolls. The dimensionless control parameter proportional to ΔT is the Rayleigh number

$$R\equiv\frac{g\alpha d^3\Delta T}{\nu\kappa}, \tag{2}$$

where α is the isobaric thermal expansion coefficient and κ is the thermal diffusivity. The inhibition of convection by rotation is illustrated in Fig. 1(a), which shows the neutral stability curve $R_c(\Omega)$ calculated from linear stability analysis [1]. The dimensionless wave number of the rolls is $k\equiv 2\pi d/\lambda$ and its value at ΔT_c is k_c. The increase of k_c with Ω is shown in Fig. 1(b). For large Ω, R_c and k_c are predicted to scale as $\Omega^{4/3}$ and $\Omega^{1/3}$, respectively [1]; for small Ω, as in the work presented here, R_c and k_c should be quadratic in Ω because of the symmetry of the convection state under reversal of the rotation direction. Previous experimental measurements of these quantities are sparse, particu-

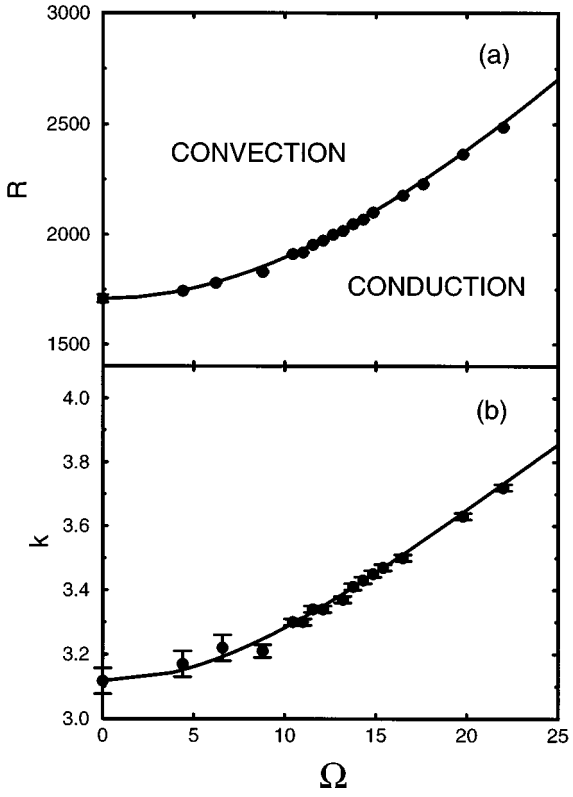

FIG. 1. (a) R_c and (b) k_c vs Ω. Solid lines are predictions of linear theory, and the data are for $\Gamma=40$.

larly for the pattern wave number because of the difficulty of visualizing convection patterns near onset in a rotating system. Measurements of R_c as a function of Ω for small rotation rates ($\Omega\lesssim 30$) that agreed semiquantitatively with theoretical predictions were reported by Rossby [6] and Zhong *et al.* [16] for water, by Bühler and Oertel using nitrogen gas [11], and by Lucas *et al.* for liquid ^{4}He [12]. In the experiments using water and for $\Omega<50$ by Zhong *et al.*, the wave number at $\epsilon\approx 0.4$ was found to agree with the theoretical prediction for k_c to within an experimental uncertainty of about 10%. This was the best determination of k_c prior to the results reported in this paper where patterns could be studied quantitatively for $\epsilon\gtrsim 0.01$. Since k_c as well as R_c can be calculated from an exact linear stability analysis, their accurate measurement is very desirable to provide a firm starting point for comparison between experiment and theory. Thus, we also show in Fig. 1 the experimental data for R_c and k_c, which will be described in detail in Sec. III. As can be seen, the agreement between experiment and theory at the *linear* level is excellent.

Above onset, the size of the stable region of infinitely extended straight-roll patterns in the $k-\epsilon$ parameter space shrinks with increasing Ω [4]. As for zero rotation, the details of the stable region depend on the Prandtl number $\sigma\equiv\nu/\kappa$ of the fluid. In particular, above a critical rotation rate $\Omega_c(\sigma)$, the region of stable straight rolls shrinks to zero, and for $\Omega\geqslant\Omega_c(\sigma)$ the straight-roll pattern becomes unstable to the Küppers-Lortz (KL) instability even at arbitrarily small ϵ [2,3]. This instability causes otherwise steady convection rolls of a given orientation to become unstable to rolls oriented at some angle advanced in the direction of rotation. Thus, the roll orientation changes in discrete steps as rolls of one orientation grow to replace rolls in the unstable direction. The angle depends on both Ω and σ [3,4] and can vary between 30° and 70°. It is, however, close to 58° for $\sigma\gtrsim 1$ and $\Omega\gtrsim 15$ [4]. Because of the close proximity of the KL angle to 60°, theoretical models have been developed that consist of equations for the amplitudes of three coupled modes. The first such model, developed by Busse and Heikes [9], explained many qualitative features of early experimental observations of the KL instability [8–10]. It was later extended to include spatial gradient terms by Tu and Cross [19]. An important result of the latter work was to demonstrate that a signature of the KL instability below Ω_c was the propagation of fronts of one orientation into roll domains of a different orientation. This helped to explain the experimental observations of front propagation [16–18] and of an apparently lower value of Ω_c than theoretically predicted [3]. Numerical solutions of generalized [20–23] Swift-Hohenberg (GSH) equations [24,25] and of the Navier-Stokes equations in the Boussinesq approximation [26] have also been used to study the KL instability.

Although the KL instability is important in many of our experimental observations, its influence is often mixed with other effects. Thus, many of the experimental results are directly comparable to theoretical models only quite close to onset and for $\Omega\gtrsim\Omega_c$ ($\Omega_c\approx 13$ for $\sigma=0.93$). Results in that parameter range are reported in detail elsewhere [27,28]. Here we present measurements over a wide ϵ range of the effects of rotation on pattern textures. These effects include wave number selection and phenomena affecting pattern dynamics such as defect nucleation and propagation. The KL instability in this context comes in through the location of its stability boundary, which, for a given wave number, moves to smaller ϵ with increasing Ω. We will divide our discussion into two parts: the first with $\Omega\lesssim 8$ is a description of textures and dynamics where the KL instability is not apparent. The second involves states for $\Omega\gtrsim 8$ where the KL instability definitely plays a role. In the first it will be important to recall what is known theoretically about secondary stability boundaries and pattern dynamics in both the nonrotating and rotating system.

For the nonrotating case, the theory for the stability of straight parallel rolls of infinite lateral extent, developed for a whole range of Prandtl numbers by Busse and Clever [29–31], has been very useful in describing experimental observations of patterns. The assumption of uniform wave number in the theory leads to the expectation that the pattern becomes unstable to a particular perturbation simultaneously everywhere in space. On the other hand, many features of real patterns that include wave-number gradients, roll curvature, and defects are not considered by such theories. However, it was realized that, to a good approximation, the long-wavelength instabilities of the laterally infinite system, such as the Eckhaus and skewed-varicose instabilities, will also occur when the *local* wave number of a pattern crosses an instability boundary. In that case the instability leads to the formation of defects that travel away and relax the extremes of local wave numbers back into the stable range. These ideas have evolved from early motivating experiments [32–37], and by considering the infinite-system instabilities in conjunction with phase equations [38–46] coupled to mean-

drift flows that are relevant for low-σ fluids [39,40]. In addition to phenomena that can be explained to some extent as ''finite-size'' perturbations of concepts from infinite-system instabilities, there are states to which the theory of straight rolls is not applicable at all. The state of spiral defect chaos (SDC) discovered by Morris *et al.* [47] (see, for instance, Fig. 11 below) is a prime example. It consists of highly curved rolls in the form of spirals and targets and exists in regions of k-ϵ space where straight, parallel rolls are known theoretically to be stable [29–31,48,49]. These states pose a significant challenge to the existing theories of Rayleigh-Bénard convection.

A number of recent experiments and numerical simulations for $\Omega=0$ and $\sigma\approx 1$ have added considerably to our understanding of real patterns. For radius-to-height ratios Γ similar to those of the present work, experiments have provided quantitative information about axisymmetric wave-number selection and the focus instability [50], nucleation rates of phase in the cores of sidewall foci [51], the nucleation mechanisms of spiral defects [52] and the transition to spiral-defect chaos [53], and the dynamics of textured patterns [54]. This work has provided an extensive characterization of pattern wave numbers, correlation lengths, roll curvatures, and sidewall obliqueness. Computer simulations of low-Prandtl-number convection using both generalized Swift-Hohenberg models [55–57] and the Navier-Stokes equations in the Boussinesq approximation [48,58] have also been extremely valuable. The experiments, simulations, and theory reveal interesting features, many of which are not understood. There are, however, some general conclusions for nonrotating, low-σ convection in cylindrical containers. First, in the absence of strong sidewall forcing, the onset pattern is time independent and consists of straight rolls throughout most of the cell with small cross-roll defects near the part of the periphery where the sidewall is approximately parallel to the roll axis in the interior [see, for instance, Fig. 8(a) below]. With increasing ϵ, the tendency for the rolls to terminate with their axes orthogonal to the circular sidewall increases [see Figs. 9(a)–9(c) below]. The resulting roll curvature in the cell interior leads to a wave-number distribution with a maximal wave-number increase near the cell center. Time dependence appears first at $\epsilon\approx 0.1$ in the form of repeated skewed-varicose dislocation-defect nucleations near the cell center followed by defect motion and pattern rearrangement [see, for instance, Fig. 9(a) below] [37,50]. Experiments [59,60] have demonstrated that mean drift driven by boundary-induced roll curvature is responsible for the observed time dependence. The appearance of SDC seems to depend on Γ in a complicated fashion [47,53,61–63], but for $20\lesssim\Gamma\lesssim 60$ and $\sigma\simeq 1$ the transition occurs at $\epsilon\approx 0.5$. The pattern dynamics in the intermediate region $0.1<\epsilon<0.5$ are dominated by the development of strong wall foci [see, for instance, Figs. 9(b) and 9(c) below], increasingly (with ϵ) vigorous dislocation-defect motion, but little change in average roll curvature or sidewall obliqueness [54]. These are the main features of pattern dynamics for nonrotating, low-σ convection. An important thing to keep in mind is that the most obvious consequence of wave-number-relaxing instabilities is the formation of a small number of defects.

We now consider stability theory and numerical simulations for rotating convection and the limited number of experimental observations of pattern dynamics for that case. For $\sigma\approx 1$, the KL and skewed-varicose (SV) instabilities at high wave number and the Eckhaus (EK) instability at low wave number are important secondary instabilities near the onset of convection [4,26]. Figure 2 shows the calculated stability boundaries for several values of Ω for $\sigma=1.0$ [64]. As Ω is increased, the major features of these curves are the stabilization of straight rolls against the skewed-varicose instability and their destabilization with respect to the Küppers-Lortz instability. The destabilization with respect to the KL instability leads to a shrinking straight-roll stability window as Ω is increased. At a critical value $\Omega_c(\sigma)$, this stability window disappears altogether and straight rolls are no longer stable at any ϵ. In contrast to the dramatic change in the SV boundary with increasing rotation, the low-wave-number boundary is practically unaffected.

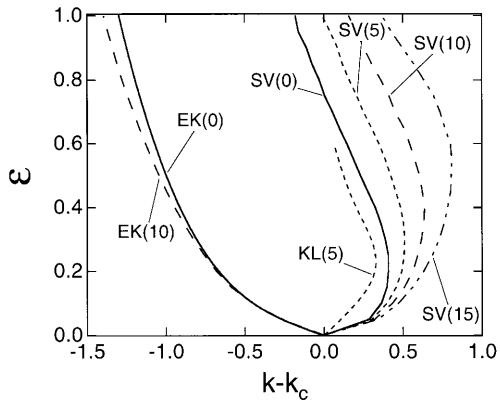

FIG. 2. Stability boundaries for straight parallel rolls with respect to long-wavelength instabilities, EK (Eckhaus) and SV (skewed-varicose), and to the Küppers-Lortz instability. $\sigma=1.0$. Values of Ω are 0 (—), 5 (- - -), 10 (– – –), and 15 (– - - –). Boundaries for different instabilities are labeled on the plot with the value of Ω in parentheses.

Another powerful approach to the study of pattern dynamics in Rayleigh-Bénard convection, which augments the secondary-stability calculations is the numerical simulation of model equations, in particular the Swift-Hohenberg (SH) equation [24,25] and its generalizations [46] to include mean drift [65], non-Boussinesq effects [66], and rotation about a vertical axis [20–22]. The models that include rotation have been used to both confirm experimental observations and make predictions regarding the behavior of patterns and defects under the influence of rotation. In relation to the experimental results presented here, a limitation of the models that have included rotation is that they are effectively large-σ models since mean drift is ignored. Nevertheless, in systems with quite different σ, the experimental observations [16–18] of sidewall-initiated front propagations caused by the KL instability, the motions of sidewall defects, and the ''S-shaped'' distortion of the straight-roll pattern have been reproduced qualitatively [20,21]. These simulations have also suggested the possible existence of rigid pattern rotation caused by defects [67] and the enhancement by rotation of the nonvariational property of dislocation glide [58,67]. Recently, a simulation of a GSH equation that included both rotation and mean drift [23] showed a number of pattern features that we observe.

The dependence of the average wave number of the patterns on ϵ as a function of Ω and close to onset has not been investigated systematically prior to our work. There are, however, several studies for higher ϵ that should be mentioned. For $\epsilon \gtrsim 3$ and depending on σ and Ω, Heikes observed hexagonal cellular patterns and cross-roll patterns composed of two perpendicular sets of rolls in water with σ between 3.8 and 14.5 in cells with $\Gamma = 60$ [8]. Heikes also measured the wave number k of the patterns from ϵ of 0.5 to about 10 [8]. The wave number decreased with increasing ϵ, in agreement with previous measurements by Rossby in silicone oil at $\sigma = 100$ [6] up to $\epsilon \approx 4$. For $\epsilon > 4$, k in water continued to decrease whereas k in silicone oil increased.

In the following section, the apparatus is described. Next, in Sec. III, we present the linear results for this system, namely, the critical Rayleigh number R_c and the critical wave number k_c as a function of Ω. In Sec. IV, we give results that can be understood in the context of secondary instabilities and with insight developed from previous work on this system with $\Omega = 0$ [27,53,54]. First we give a summary of the different states in the parameter space of ϵ and Ω. Of particular interest here are the motions of defects, the overall pattern textures, and the persistence of the spiral-defect-chaos state under rotation. We then discuss the influence of the skewed-varicose instability on the system and give measurements of the characteristic angle associated with it as a function of Ω. A more detailed discussion of the motion of defects for $\Omega > 0$ is then given, and their overall effect on pattern rotation relative to the rotating frame of the experiment is presented. In Sec. V quantitative results for the average wave number, correlation length, roll curvature, and sidewall obliqueness of the patterns are given as a function of Ω and ϵ. In Sec. VI, pattern dynamics for each of the regions identified in parameter space are presented in the form of image sequences. We conclude in Sec. VII with a summary.

II. EXPERIMENTAL APPARATUS AND PROCEDURES

The apparatus is described thoroughly elsewhere, [47,50,68] as are details of the cell construction and procedures for determining ΔT_c [50,54]. The circular sidewall used in the majority of studies reported in this paper ($\Gamma = 40$) had a cross section shaped like the letter H and enclosed an active convective area measuring 86 mm in diameter [69]. This H-shaped design minimized the sidewall thickness seen by the fluid and reduced the effect of sidewall forcing [50]. Despite this design, two to three concentric rolls were visible next to the sidewall when ΔT was about 1% below the value at which the center of the cell started convecting. This, however, did not affect the determination of ΔT_c (see Sec. III) significantly. The sidewall was sandwiched from the top by a 9.5-mm-thick optically flat sapphire window and the bottom by an aluminum plate with mirror finish. The spacing between the window and plate determined the layer height d, but owing to an *in situ* adjustment of the uniformity of d to within 0.002 mm, the absolute value of d could not be measured directly. We inferred it indirectly through a comparison of ΔT_c at $\Omega = 0$ with that of a calibration cell with a known cell height operated at the same temperature and pressure [70], and through the assumption that at onset the wave number of the straight-roll structure was the critical wave number $k_c = 3.117$. These two methods gave the same $d = 1.06$ mm with an uncertainty of 1%, and a radius-to-height ratio Γ of 40. The cell was filled with CO_2 at 33.1 bars, and the temperature of the bath that cooled the top plate was held constant within $\pm 0.0002\,^\circ$C over periods of a week or longer near 33.70 °C. Under these conditions, the fluid had a Prandtl number of 0.93. The pressure was regulated by a temperature-controlled external ballast volume to within 0.005%. The vertical thermal diffusion time $\tau_v = d^2/\kappa$ was 4.5 sec, and the horizontal thermal diffusion time $\tau_h = \Gamma^2 \tau_v$ was 7200 sec. The measured $\Delta T_c(\Omega = 0)$ was $1.487 \pm 0.004\,^\circ$C. From Eq. (2) and $R_c = 1708$, we estimate $\Delta T_c = 1.47\,^\circ$C, which agrees with the experimental value well within reasonable estimates of errors in d and in the fluid properties [68] that we used.

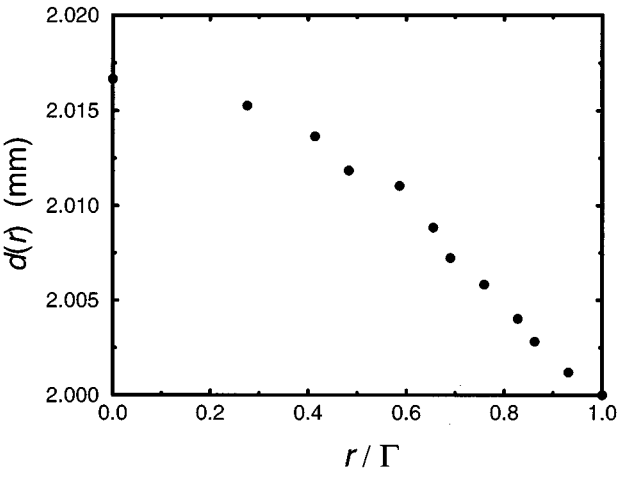

FIG. 3. The thickness $d(r)$ as a function of the radial position r (in units of d) for the cell with $\Gamma = 23$.

We also made some measurements in a cell with $d = 0.201$ cm and a correspondingly smaller aspect ratio $\Gamma = 23$. For this case, the sidewall was made of Macor, a machinable ceramic. It was 0.200 cm thick and had a ''spoiler tab'' [50,71,72] that was intended to reduce thermal sidewall forcing. In this cell, a thinner sapphire window (3.2 mm) was used for the cell top. This resulted in a slight bowing of the cell in the middle owing to a small pressure differential between the sample and the water bath. Thus the cell profile was approximately axisymmetric with maximum height at the center. This caused the convection pattern to grow in from the center where the effective ϵ was highest and had the consequence of reducing sidewall effects near onset, albeit at the price of a small spatial ramp in ϵ. By measuring the radial location r where the pattern was first noticeable as a function of ΔT, we estimated the local cell thickness $d(r)$. The result is shown in Fig. 3. As can be seen, d varied by 0.8% across the radius, leading to a total variation of ϵ of 2.4%. For this cell the bath temperature was also 33.70 °C, but the pressure was 16.55 bars. Using the method described in Sec. III, we measured ΔT_c to be 1.557 °C. Using this value as corresponding to $\epsilon = 0$, convection first started in the cell center at $\epsilon = -0.015$, and the cell was completely filled with convection for $\epsilon \geqslant 0.012$. On the basis of the data in Fig. 3 we estimate that the value of d corre-

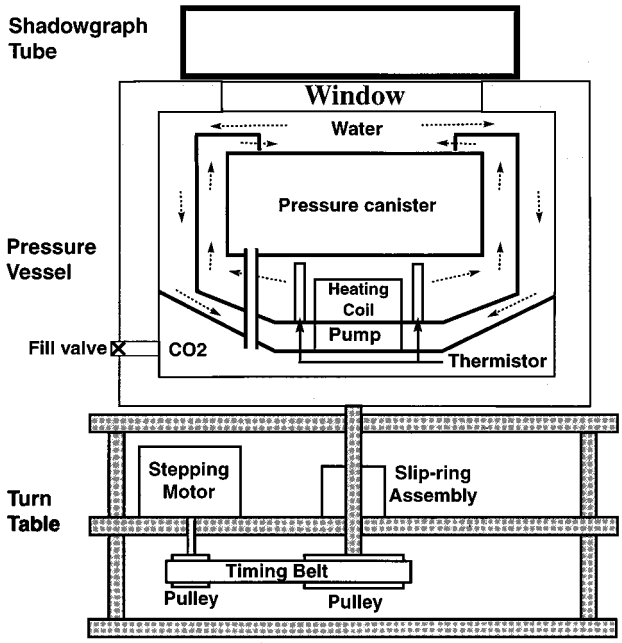

FIG. 4. Schematic diagram of the apparatus.

sponding to the radial onset location for $\Delta T=\Delta T_c$ is $d=0.201$ cm. With Eq. (2) and the known fluid properties [68] this yields $\Delta T_c=1.54$ °C, in very good agreement with the experiment. For this cell, τ_v was 6.7 sec and σ was 0.83. It follows that a particular value of Ω is reached at a dimensioned rotation rate f, which is smaller than in the larger-Γ cell by a factor of about 1.68 (the ratio of the values of τ_v/σ). Since the centrifugal acceleration is proportional to f^2, it was smaller by a factor of about 2.81 at a given Ω in the thicker cell. This cell gave essentially equivalent results wherever a comparison with the larger cell could be made except very close to onset as described below.

Convection in both of the cells was well approximated by the Boussinesq approximation. The parameter $\mathcal{P}$ defined by Busse [73] that describes the size of departures from the Boussinesq approximation is 0.17 and 0.10 for the $\Gamma=40$ and 23 cells, respectively. Non-Boussinesq effects in a similar system but with smaller layer depth have been studied carefully [74].

The cell was placed inside a pressure vessel that was mounted on a turntable with the electrical connections routed through a slip-ring assembly concentric with the rotation axis. A schematic illustration of the arrangement of the major components of the apparatus is shown in Fig. 4. A microstepping controller drove a stepping motor that rotated the turntable through a belt-and-pulley arrangement with one revolution of 360° completed in 50 000 microsteps. The top rotation rate achievable with this setup was limited by air friction and stepping-motor power. For the $\Gamma=40$ cell, 1 Hz was equivalent to $\Omega=30$. The effect of the centrifugal force at the highest rotation rate in the experiments of 0.7 Hz was small, with $(2\pi f)^2\Gamma d/g=0.09$. The rotation direction is specified as seen when viewed from above and is counterclockwise (positive Ω) for all the results reported in this paper.

The convection patterns were observed by the shadowgraph visualization method with the necessary optics contained inside a cylindrical tube mounted on top of the pressure vessel. The tube rotated with the cell, so observation of patterns was in the rotating frame of reference. The shadowgraph images were captured and digitized as 8-bit grey-scale-coded images. In this paper, the contrast-enhanced images show black regions corresponding to hot fluid (upflow) and white regions corresponding to cold fluid (downflow). For the work discussed in the present paper, approximately 200 000 images were analyzed.

The complex spatial and temporal dynamics of the patterns made quantitative analysis challenging. Here we used the same algorithms presented in Ref. [54] to characterize these dynamical patterns. To describe the spatial scales of the patterns, the first two moments $\langle k\rangle$ and ξ^{-2} were obtained from the structure factor $S(k)$, which was calculated by squaring the modulus of the Fourier transform $F(\mathbf{k})$ [47,54]. In the computation of the Fourier transform, the Hanning window described elsewhere [54] was used. Averages of $S(k)$ were computed over image sequences taken at fixed Ω and ϵ, with each sequence containing between 128 and 256 images equally spaced in time. The time interval at each ϵ was adjusted so that the images were uncorrelated except for $\epsilon\lesssim 0.1$ where the time scale of the dynamics was very long. The physical interpretation of $\langle k\rangle$ is that of the average pattern wave number but that of ξ is much less obvious. The width of the distribution depends on the roll curvature, the number of defects, wave-number gradients, and the size of domains (a spatial region with roughly uniform pattern texture) in a complicated manner [75,76]. It is, however, a simple and well-defined measure of spatial order disorder and as such we use it here.

Measures of the pattern texture are the roll curvature and sidewall obliqueness. These were extracted from each image by locally fitting the roll to a parabola in the interior and a straight line near the wall, respectively [54]. Unfortunately, these real-space techniques were not suitable for cellular regions with coexisting rolls and defects or for regions near KL fronts. Thus, they were primarily used to characterize patterns at small rotation rates, $\Omega\lesssim 8$, where cellular regions appeared infrequently, and KL fronts did not occupy a significant fraction of the total area. The roll curvature γ measures locally the amount of angular change per unit length along the rolls, and the spatially and temporally averaged curvature $\gamma_{s,t}$ is the average over all the images in the same sequence. The similarly averaged sidewall obliqueness $\beta_{s,t}$ is based on roll orientations in the area adjacent to the sidewall. It provides a measure of the average deviation from perpendicular termination of the roll axes at the sidewall.

III. LINEAR RESULTS FOR $\Delta T_c(\Omega)$ AND $K_c(\Omega)$

Heat-transport measurements and simultaneous shadowgraph visualization allow for the experimental determination of R_c and k_c. The critical temperature difference is obtained from Nusselt-number data. The Nusselt number $\mathcal{N}$ is defined as the ratio of total heat conducted by the fluid in the convecting state to that conducted only by thermal diffusion. An example for $\Gamma=40$ at $\Omega=15.4$ of typical results for $\mathcal{N}$ is shown in Fig. 5. There is a small region of rounding for $-0.01\lesssim\epsilon\lesssim 0.01$ ($1.865\,°\text{C}\lesssim\Delta T\lesssim 1.895\,°\text{C}$). In principle,

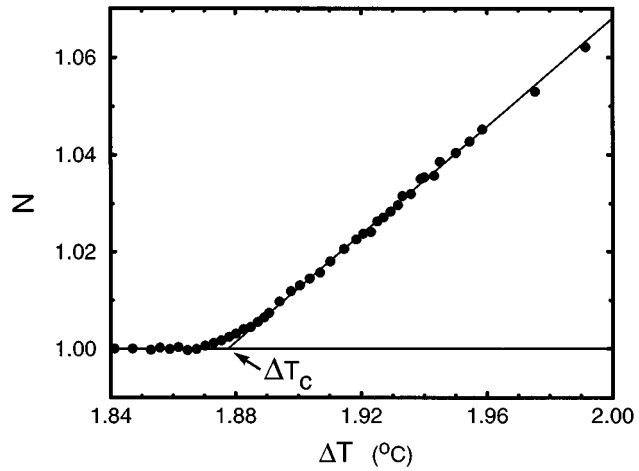

FIG. 5. Nusselt number vs ΔT for the determination of ΔT_c. $\Omega = 15.4$ and $\Gamma = 40$. The solid lines are least-squares fits to the data below and above ΔT_c outside the rounded region.

rounding at some level would be expected from large-scale flows induced by the centrifugal acceleration. In our experiments, however, the rounding was of the same size at all Ω including $\Omega = 0$. Thus, we attribute it to experimental imperfections in the convection cell and conclude that centrifugal effects on $\mathcal{N}$ were much less than revealed by the data in Fig. 5.

Away from the rounded region we fit the function

$$\mathcal{N} - 1 = S_1 \epsilon + S_2 \epsilon^2 \tag{3}$$

to the data for $\mathcal{N}$ in the convecting region. In the fit, ΔT_c, S_1, and S_2 were adjusted. From the results for ΔT_c we computed R_c using the fluid properties evaluated at the mean cell temperature. Figure 1(a) shows the results for $R_c(\Omega)$ as well as the prediction based on linear stability analysis [1]. The agreement between the data and the prediction is excellent. A different way to illustrate this agreement and to show the quadratic dependence of R_c on Ω is to plot $R_c(\Omega)/R_c(0)$ against Ω^2 as in Fig. 6(a), where results for both cells are given. The dashed line is drawn with the initial slope of the theoretical results, and illustrates that noticeable deviations from the quadratic relationship occur for $\Omega \gtrsim 10$.

We determined k_c for rotating patterns from Fourier transforms of shadowgraph images. As discussed in Sec. II, the wave number at onset for $\Omega = 0$ is assumed to be $k_c = 3.117$. For nonzero Ω we determined k_c from an extrapolation of the average wave number $\langle k \rangle$ as a function of ϵ for $\epsilon \lesssim 0.1$ (see Fig. 30 below). In Fig. 1(b) the experimental results for the $\Gamma = 40$ cell are seen to agree well with the predictions from linear stability analysis. Again one can demonstrate the quadratic scaling for small Ω by plotting $k_c(\Omega)/k_c(0)$ versus Ω^2 as is done in Fig. 6(b) for both cells.

IV. NONLINEAR STABILITY

The behavior of patterns as a function of rotation depends on many influences and is extremely complicated in detail. From previous experiments without rotation on large-Γ cells and for $\sigma \simeq 1$ [27,37,51,53,54], and from a large amount of theoretical and numerical modeling [46], we know that the

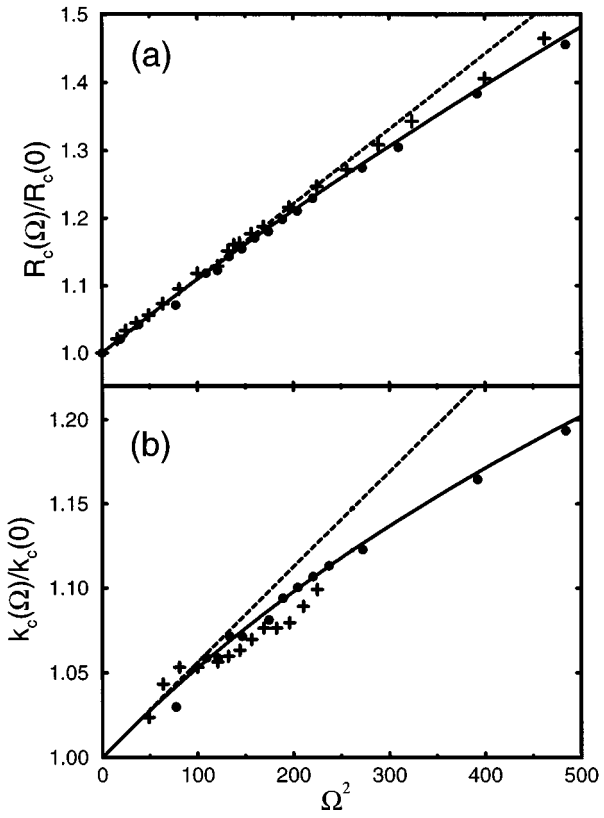

FIG. 6. (a) $R_c(\Omega)/R_c(0)$ and (b) $k_c(\Omega)/k_c(0)$ vs Ω^2. Solid lines are predictions of linear theory and the dashed lines are the initial slopes of the theoretical curves. The data are for $\Gamma = 40$ (●) and $\Gamma = 23$ (+).

dynamics of patterns for $\Omega = 0$ is governed by a complex interaction of long-wavelength instabilities (Eckhaus, skewed-varicose, etc.), large-scale vertical-vorticity modes (mean drift), and interactions with the convection-cell lateral boundaries. A complete picture has not been established, partly because of the difficulty in directly measuring the mean-drift field. To this we add rotation. Clearly, we cannot achieve a full characterization of pattern dynamics in rotating convection. What we will describe are phenomena for which a reasonable picture could be developed based on concepts from the nonrotating problem or that were seen many times and were somehow generic to the convecting state at particular parameter values. In reporting quantitative measures of patterns, we nondimensionalize length scales with d and time scales with τ_v.

One general feature of the rotating system is that the lateral boundaries become more important than for the nonrotating case. Previous experimental work [16] and subsequent numerical models [20] showed that even for small rotation, defects could be nucleated at and travel along the sidewalls (at higher rotation, the wall has such a dominant effect that a new wall state becomes unstable at a smaller R than R_c for the bulk state [77]). In the present work we also observe many sidewall defect nucleations and defect motions, which we describe in detail. These wall-generated defects make comparisons with theories problematic since most treatments consider either a laterally infinite system, or a large-aspect-ratio limit where sidewalls should have only a small influ-

ence. Theoretical analysis will have to include realistic sidewall interactions because experimentally sidewall effects cannot be avoided merely by increasing lateral system size. However, we will make some comparisons between data for the $\Gamma=40$ cell and the $\Gamma=23$ cell that had a slight axisymmetric ramp of ϵ as described in Sec. II. The ramp caused convection rolls to form in the interior of the cell before they formed near the walls. This isolated the bulk state from sidewall influences for a small range of ϵ and had a simplifying effect on the pattern dynamics over that range.

Another difficulty in analyzing our experimental results is that the theoretical and numerical modeling of pattern dynamics in rotating convection is not nearly as extensive as for nonrotating convection although there has been a flurry of recent activity [20,21,58,67]. For example, whereas the stability boundaries for nonrotating convection are known in detail for arbitrary σ owing to the large body of work by Busse and co-workers [73], the only published work on the effects of rotation [4] has almost no data for $\sigma=1$. Although some recent work [26] is beginning to fill that gap, a complete characterization of secondary stability boundaries as a function of rotation is not available. Nevertheless, as the concept of secondary stability has proven so valuable for nonrotating convection, we apply it here as best we can.

There are two influences of rotation on secondary instability: the shift of stability boundaries present without rotation and the introduction of new rotation-induced instabilities. In Fig. 2, the long-wavelength instability boundaries that are present also without rotation are shown for several rotation rates. There is not much effect of rotation on the low-wave-number boundaries for $\Omega\lesssim 15$; for $\Omega=20$ the Eckhaus boundary at small $\epsilon\lesssim 0.3$ is replaced by the cross-roll instability. On the high-wave-number side the effects of rotation are more dramatic since the SV boundary is shifted to higher wave number as Ω increases. This suggests that the SV instability should be less relevant to the dynamics at higher Ω. Another result of this analysis is that the angle for the SV instability decreases with rotation [26].

The rotation-induced Küppers-Lortz instability emerges as Ω is increased and is usually associated with the critical rotation rate Ω_c. But just as the skewed-varicose instability has a big influence on pattern dynamics before the SV boundary is actually crossed by the mean wave number because of pattern textures with roll curvature and wave-number gradients, one might expect that the KL instability would have a similar effect for $\Omega<\Omega_c$. In Fig. 2, the shrinking domain of stability in wave-number space is shown for different Ω. For $\Omega<4$, the long-wavelength instabilities are important, and the KL instability should play little part in the pattern dynamics. For $\Omega>4$ the KL-limited region is smaller than the long-wavelength-limited one and KL dynamics should dominate. We will revisit this issue later and plan to discuss it as well in another paper focusing on the KL dynamics [28]. One would expect from this theoretical analysis that, even for modest Ω, KL dynamics would be preferentially observed relative to other dynamics related to long-wavelength straight-roll instabilities. It may be difficult, however, to distinguish the signature of the KL instability, when it occurs locally, from that of other instabilities. Before delving into specific signatures of secondary instabilities, it is useful to give an overall representation of the different pattern textures that one sees in different regions of parameter space.

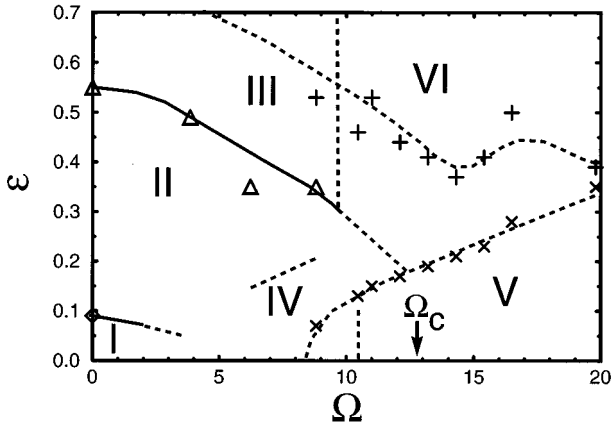

FIG. 7. Phase diagram in the ϵ-Ω parameter space for $\Gamma=40$ and $\sigma=0.93$. The division into regions was done by visual observation of the patterns, in some cases supplemented by quantitative measurements. Symbols representing these determinations are SV ($\diamond$) and SDC ($\triangle$). Solid lines denote known boundaries whereas dashed lines are interpolations or suggestions of boundaries. Additional data for the boundaries ϵ_1 and ϵ_2 for the linear dependence of the average wave number on ϵ (see Fig. 30 below) are shown as crosses and plusses, with dashed lines to guide the eye.

A. The big picture

The parameter space shown in Fig. 7 can be roughly divided into six regions based on the types of patterns that are observed. The determinations of the boundaries of those regions are approximate because the coexistence of behaviors attributable to different instabilities was observed over large parts. Some of the data indicate boundaries between regions of linear variation with ϵ of the average pattern wave number [see Sec. V and Fig. 30(b) below] that is roughly correlated with some of the overall pattern dynamics we observe. In region I, for $\Omega\lesssim 3$ and $\epsilon\lesssim 0.1$, the pattern consisted of straight or gently curved rolls that were time independent at the onset of convection (Fig. 8). These straight rolls were bounded on roughly opposite sides by a short region of a cross-roll grain boundary (not to be confused with the cross-roll instability). At slightly higher Ω, the issue of time dependence near onset was complicated by the nucleation of

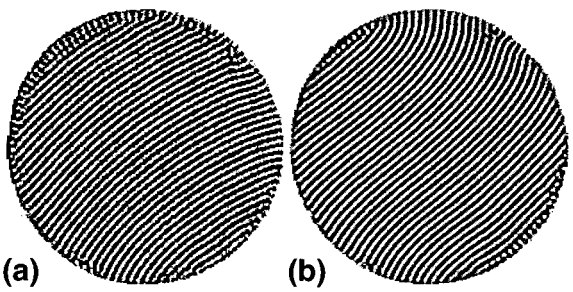

FIG. 8. Representative patterns for (a) $\Omega=0$, $\epsilon=0.04$ and (b) $\Omega=4.4$, $\epsilon=0.04$ illustrating straight or slightly curved convection rolls in region I. For (b), the overall pattern rotation is counterclockwise, and the short cross rolls travel in the clockwise direction.

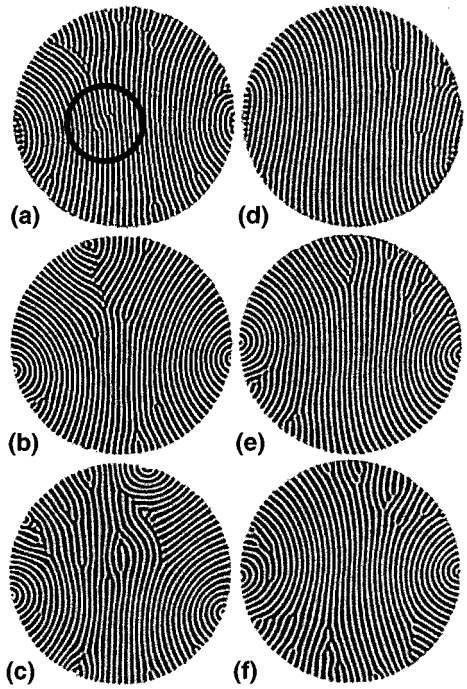

FIG. 9. Representative patterns from region II for (a) $\Omega=0$, $\epsilon=0.12$, (b) $\Omega=0$, $\epsilon=0.25$, (c) $\Omega=0$, $\epsilon=0.44$, (d) $\Omega=3.9$, $\epsilon=0.13$, (e) $\Omega=3.9$, $\epsilon=0.29$, and (f) $\Omega=3.9$, $\epsilon=0.44$. The enclosed region in (a) identifies a SV defect pair.

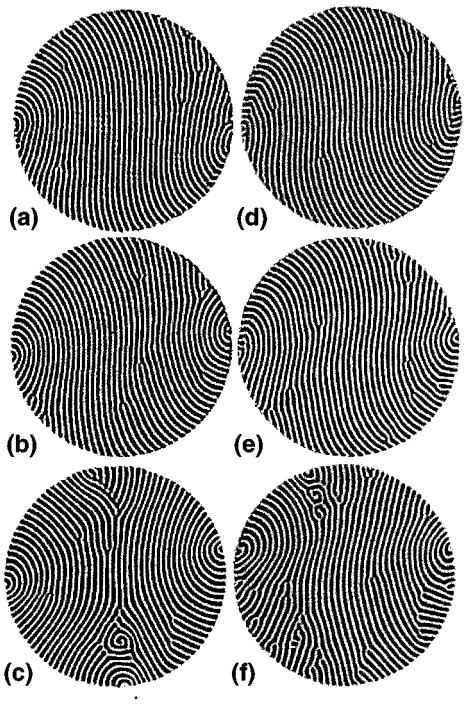

FIG. 10. Representative patterns from region II for (a) $\Omega=6.2$, $\epsilon=0.15$, (b) $\Omega=6.2$, $\epsilon=0.25$, (c) $\Omega=6.2$, $\epsilon=0.35$, (d) $\Omega=8.8$, $\epsilon=0.16$, (e) $\Omega=8.8$, $\epsilon=0.25$, and (f) $\Omega=8.8$, $\epsilon=0.35$. Patterns in (c) and (f) have small spiral defects that indicate that these parameter values are quite close to the SDC onset.

defects at the sidewalls and the interaction of sidewall forcing with such nucleations. Images for the $\Gamma=23$ cell in which much more data were taken for small ϵ helps to elucidate this behavior, but we postpone this discussion until later. In region II, the patterns were similar to the nonrotating patterns and had an ''S-shaped'' (SS) distortion of the straight rolls. Representative samples of images in region II are shown in Figs. 9 and 10. The SS distortion appears to be a generic response of straight rolls to rotation, as observed also in experiments at larger Prandtl numbers [17,18] and noted in GSH simulations [20] for which σ is effectively infinite. The degree of distortion increases with Ω as illustrated in Figs. 9(d) and 10(a) and 10(d). An observation related to the SS distortion is that the large sidewall foci on opposing sides of the cell were not as symmetrical as the ones at $\Omega=0$ [Fig. 9(b)]. At $\Omega=8.8$ [Fig. 10(e)], the asymmetry of the sidewall foci became very pronounced. On the side clockwise from the foci, rolls ended nearly perpendicular to the sidewall whereas on the other side rolls were almost parallel to the sidewall. Since the direction of rotation was counterclockwise, it was the side opposite to the rotation sense that contained rolls ending perpendicular to the wall.

The other general aspect seen in region II was the nucleation and motions of dislocation defects. The defects were nucleated both in the bulk and near the sidewall and were sometimes identifiable as arising from either the Eckhaus or skewed-varicose instabilities. An example of a SV nucleated pair of defects is illustrated in Fig. 9(a). There are many instances, however, especially at higher Ω, when the mechanism for defect nucleation was not clear, and the only thing that could be determined was whether it was a wave number increasing or decreasing nucleation. Further, it is not clear whether the concept of laterally infinite long-wavelength instability applies in the presence of other defects or near the walls. Thus, we will sometimes refer to specific nucleation mechanisms and at other times to a general defect nucleation of unknown origin. The other type of defect that appeared infrequently for ϵ values that bounded region II from above were small spiral defects [Figs. 10(c) and 10(f)]. The appearance of these spirals indicates the border with region III.

Spiral-defect chaos, which was observed for $\epsilon\gtrsim 0.55$ at $\Omega=0$ [53,54], was the distinguishing feature of region III. The SDC onset for $\Gamma=40$ decreased with increasing Ω, consistent with results for a slightly larger cell with $\Gamma=52$ [63,78]. Patterns illustrative of the SDC state with and without rotation are shown in Fig. 11. The trends with increasing rotation are that the spirals become smaller, that they become predominantly counterclockwise in their winding sense [78,63] in alignment with the external rotation direction, and that the spirals become more multiarmed. Spirals for $\Omega>8.8$ were more angular in appearance [Figs. 11(e) and 11(f)]. At $\Omega=12.1$, the pattern contained mostly small target defects (a locally axisymmetric pattern of concentric rolls) rather than spirals, and spirals were seldom larger than $4d$ in diameter. Similar patterns full of target defects were observed at higher Ω. As there were no longer recognizable spirals, the ''existence of spirals'' criterion indicates that SDC did not exist for $\Omega\gtrsim 13$ and this criterion rather arbitrarily marks the boundary between regions III and VI. On the other hand certain average properties such as the linear scaling of $\langle k\rangle$ with ϵ described below seemed to continue smoothly across both regions, indicating that the state with many spiral defects at $\Omega=0$ was transformed continuously

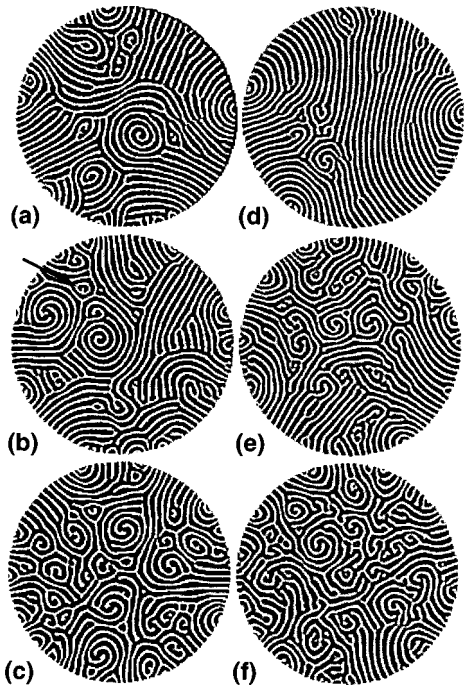

FIG. 11. Representative patterns from region III for (a) $\Omega=0$, $\epsilon=0.69$, (b) $\Omega=3.9$, $\epsilon=0.60$, (c) $\Omega=3.9$, $\epsilon=0.81$, (d) $\Omega=8.8$, $\epsilon=0.40$, (e) $\Omega=8.8$, $\epsilon=0.59$, and (f) $\Omega=8.8$, $\epsilon=0.82$. The arrow in (b) points to a target defect.

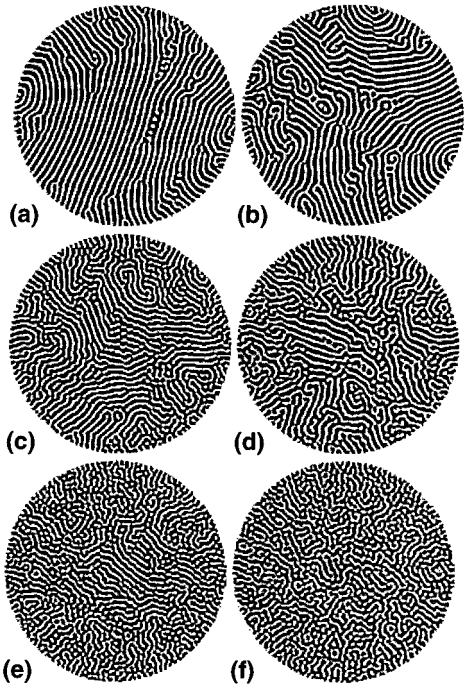

FIG. 12. Representative patterns from region VI for (a) $\Omega=12.1$, $\epsilon=0.37$, (b) $\Omega=12.1$, $\epsilon=0.54$, (c) $\Omega=15.4$, $\epsilon=0.30$, (d) $\Omega=15.4$, $\epsilon=0.62$, (e) $\Omega=19.8$, $\epsilon=0.43$, and (f) $\Omega=19.8$, $\epsilon=0.60$.

into a disordered state without spirals for large Ω. The difficulty arises in the label of ''spiral-defect chaos,'' which by definition must include spirals. In any event, the overall patterns in region VI had features reminiscent of the SDC state as shown in Fig. 12. Whether one labels this SDC or not is somewhat a matter of preference.

At intermediate Ω in region IV, the time dependence near onset consisted of a mixture of KL fronts and dislocation defects (Fig. 13). At higher ϵ, the KL instability was suppressed, and dislocation defects became dominant in region II. For $8\lesssim\Omega\lesssim10.5$ and near onset, the dynamics were a combination of dislocation-defect motion and KL-front propagation with the fronts being nucleated near the sidewall. The KL fronts were initiated by cross rolls at the sidewall and grew into the unstable central region of the cell, a process similar to observations by Zhong *et al.* [16] in a $\Gamma=10$ and $\sigma=6.4$ system. Three such fronts are visible in the images in Fig. 13 with the distinguishing features being that the fronts are curved outward in their propagation direction and that only a small number of fronts are present at the same time. The coexistence of isolated defects and KL fronts can be seen in Fig. 13(b). Another feature not shown here is that KL fronts could disintegrate into isolated defects for different parameter values. Fronts appearing spontaneously away from the wall were the distinguishing new feature of region V in Fig. 14 for $\Omega\gtrsim10.5$. This value is somewhat less than the theoretically predicted KL instability threshold at $\Omega_c=13$ for $\sigma=0.93$ [3,79]. The result of front nucleation away from the wall was that the average size of a ''patch'' (region occupied by neighboring rolls of similar orientation) was smaller compared to those in region IV where the whole cell often appeared as a single patch. The number of patches and dislocation defects grew as Ω increased. For $\Omega>15$, the number of patches became quite large, and parts of the patterns where two sets of differently oriented rolls coexisted appeared cellular, as seen in Figs. 14(c)–14(f). The cellular regions were not fixed in space as both their size and shape evolved via KL fronts, causing different regions to appear cellular at different times. The basic characteristics of patches and cellular regions remained the same up to the highest measured value of Ω ($\Omega=20$).

At very high $\epsilon\approx3$, the oscillatory instability was observed for $\Omega\lesssim12.1$ (data at larger Ω were not gathered at such high ϵ values). The instability caused the appearance of traveling waves that propagated along the rolls [37,54], and their dynamics were similar to observations at $\Omega=0$ with the waves on rolls that ended at the sidewall traveling toward the wall [54].

The details of the time independence near onset in our $\Gamma=40$ cell for small rotation rates is complicated by sidewall

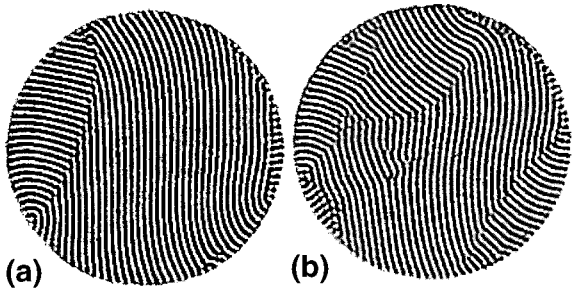

FIG. 13. Representative patterns from region IV showing wall-nucleated KL fronts. (a) $\Omega=6.2$, $\epsilon=0.07$ and (b) $\Omega=8.8$, $\epsilon=0.06$. Notice the localized cross rolls in (a) and (b).

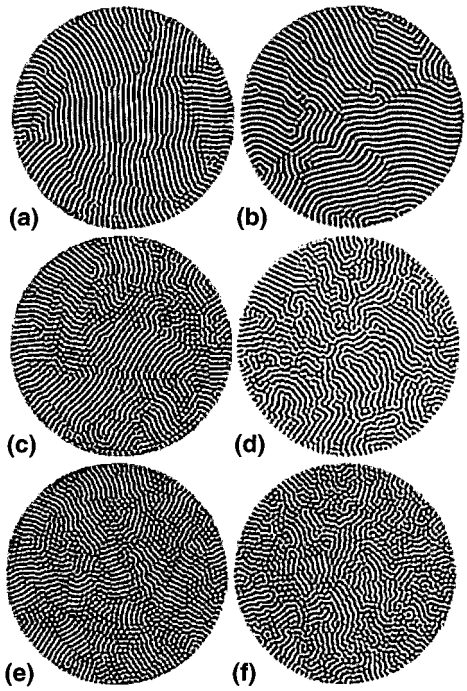

FIG. 14. Representative patterns from region V for (a) $\Omega=12.1$, $\epsilon=0.06$, (b) $\Omega=12.1$, $\epsilon=0.20$, (c) $\Omega=15.4$, $\epsilon=0.05$, (d) $\Omega=15.4$, $\epsilon=0.20$, (e) $\Omega=19.8$, $\epsilon=0.05$, and (f) $\Omega=19.8$, $\epsilon=0.18$.

effects for $\epsilon\lesssim 0.03$. Sidewall forcing in this cell induced several concentric rolls that interacted with the mostly straight roll pattern in the cell interior. In the presence of rotation, this interaction would often nucleate dislocation defects that produced some time dependence. Similarly, in region IV close to onset, KL fronts would begin from sidewall-defect structures. One is tempted to speculate that in the absence of walls, the interior structure would be time independent. Some support for this conjecture is obtained from experiments using the cell with $\Gamma=23$. In that cell there was a slight radial variation of ϵ (see Sec. II) that caused the convection pattern to form first at the center where the effective ϵ was 2.4% higher than near the wall. This had the consequence of reducing sidewall effects near onset, albeit at the price of a ramp in ϵ. Some representative images for $\Gamma=23$ are shown in Fig. 15. In Fig. 15(e), a time-independent pattern very close to onset ($\epsilon=0.01$) and at the fairly large $\Omega=11.5$ is shown with SS rolls in the interior and no visible convection near the sidewalls. With this reduced sidewall influence the phase diagram at low ϵ is modified as shown in Fig. 16. In Fig. 15(f), another pattern very close to onset with $\epsilon=0.001$ and $\Omega=12.0$ shows interior KL fronts, again with no rolls near the sidewall. Note that, in contrast to the continuous transition from sidewall KL fronts to interior generation of KL boundaries seen for $\Gamma=40$, the onset of the KL instability as a function of Ω for $\Gamma=23$ is much sharper and in quite good agreement with the theoretical prediction of $\Omega_c=12$ for $\sigma=0.83$. From these results it is apparent that defects nucleated near the sidewall have a big impact on the overall pattern dynamics near onset. Somewhat above onset, however, the patterns observed in the

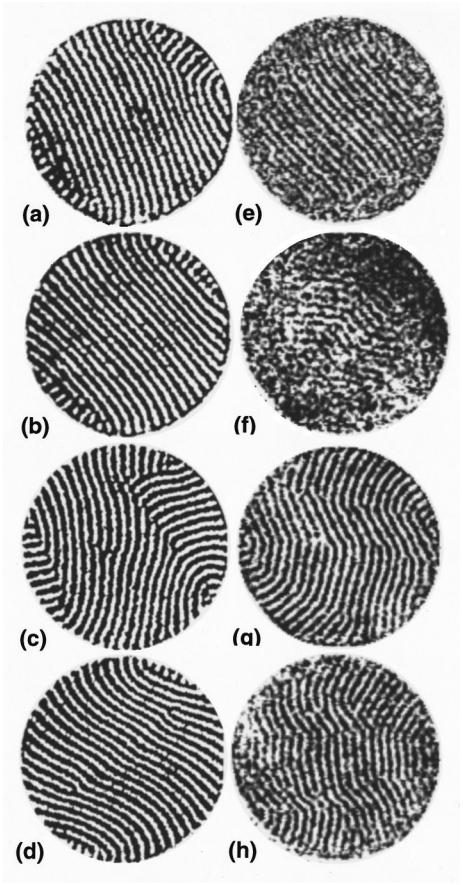

FIG. 15. Representative patterns at $\Gamma=23$ for (a) $\Omega=4$, $\epsilon=0.07$, (b) $\Omega=4$, $\epsilon=0.10$, (c) $\Omega=8$, $\epsilon=0.10$, (d) $\Omega=8$, $\epsilon=0.13$, (e) $\Omega=11.5$, $\epsilon=0.01$, (f) $\Omega=12$, $\epsilon=0.001$, (g) $\Omega=12$, $\epsilon=0.04$, and (h) $\Omega=14$, $\epsilon=0.03$.

smaller aspect ratio (Fig. 15) are quite similar to those for $\Gamma=40$.

B. Skewed-varicose instability

The SV instability dominates low-σ convection and leads to wave-number selection through the nucleation of disloca-

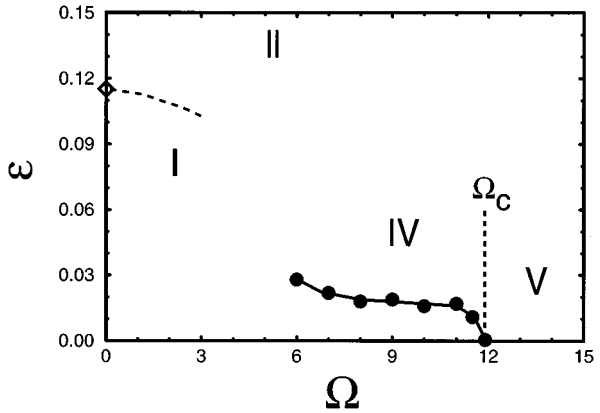

FIG. 16. Phase diagram in the ϵ-Ω plane for $\Gamma=23$ and $\sigma=0.83$. The symbols indicate actual points at which the instabilities appeared when ϵ was increased: KL (●) and SV (◇). The dashed line indicates an approximate boundary for the instabilities.

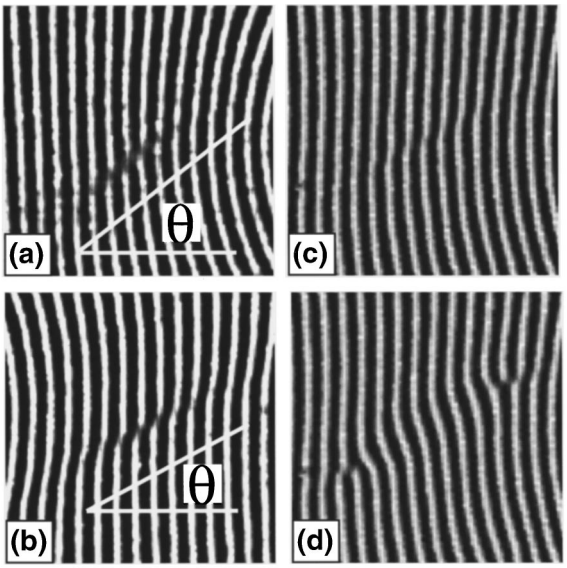

FIG. 17. Representative patterns of the skewed-varicose instability for (a) $\Omega=0$, $\epsilon=0.12$, (b) $\Omega=3.9$, $\epsilon=0.19$, (c) $\Omega=6.2$, $\epsilon=0.14$, and (d) same as (c) but $6.7\tau_v$ later.

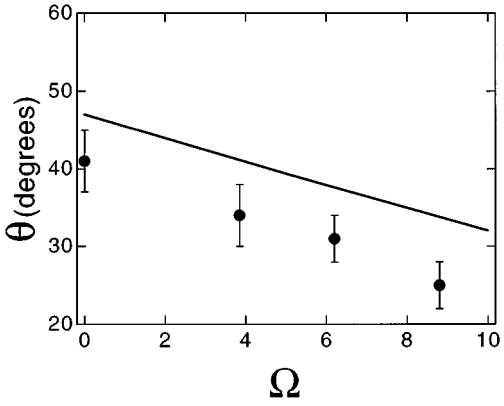

FIG. 18. The skewed-varicose instability angle θ vs Ω for ϵ near 0.15 ($\Omega=0$, $\epsilon=0.11$; $\Omega=0$, $\epsilon=0.19$; $\Omega=0$, $\epsilon=0.13$; $\Omega=0$, $\epsilon=0.16$). The data (●) were measured as shown in Fig. 17, and the solid line is the theoretical prediction for $\epsilon=0.1$.

tion pairs. Mean drift plays a crucial role in the pattern dynamics that result. For our system, the SV instability is observed frequently for $\Omega=0$ but becomes less obvious as Ω is increased. Nevertheless, rotation has a definite effect on details of the SV instability, and one observes SV defect-pair nucleations throughout region II. Here we consider characterizations of the SV instability with and without rotation, which includes the rate of dislocation-defect separation, the distortion area, and the SV angle.

In the theory of this instability [40,73], there is an angle associated with the small-amplitude, long-wavelength perturbation that has components q_x and q_y where the wave vector of the straight rolls is in the x direction. For $\Omega=0$ the angle $\arctan(q_x/q_y)$ is about 45° at $\epsilon\approx0.1$ and decreases slowly with increasing ϵ. In the presence of rotation, the angle is expected to decrease as Ω is increased at constant ϵ [64]. In experiments, the manifestation of the SV instability is a pair of dislocation defects nucleated along a line that is oriented at an angle with respect to the local straight-roll wave-vector direction. A comparison can be made between the theoretical prediction and experimental results at different rotation rates by defining an angle associated with SV defect-pair nucleations as illustrated in Fig. 17: θ is the angle between the local wave vector and the line along which the roll pinching manifests itself. In the early stages of the defect pair nucleation the roll-pinching line is one of small amplitude (notice the fuzzy region in Fig. 17) whereas later the line connects the two dislocations. Taking an average over a small number of events for $\epsilon\approx0.15$ yields the SV angle as a function of Ω (Fig. 18). Also included in the plot as a solid curve is the calculated angle for $\epsilon=0.1$. Because θ also depends on ϵ, the variation of ϵ between the different Ω values might be important. Quantitatively, however, the ϵ variation of θ yields a shift that is well within the plotted error bars and as such we ignore it. The rate of decrease of the SV angle with increasing Ω seen in the data agrees quantitatively with the calculation. The magnitude of the angle is systematically lower by about 7°. This could arise from comparing the results of a calculation valid for infinitesimal amplitude and large spatial extent to an experimental observation with large-amplitude variations on a small spatial scale. An interesting aspect of the SV instability is that, without rotation, the dislocation pairs had either a positive or negative angle of equal magnitude with respect to the rolls with apparently equal probability. Rotation removed this degeneracy and selected a particular sign of the angle that depended on the sign of Ω. This phenomenon is related to the influence of rotation on the motion of isolated defects, which is discussed in the next section. Finally we note that the images of Croquette (Fig. 22 of Ref. [37]) for $\Omega=0$, $\sigma=0.69$, and $\epsilon=0.085$ suggest an angle of about 90°, where the defects move apart by a nearly pure climbing motion. This behavior would be expected for the Eckhaus instability.

In the absence of rotation, SV-nucleated defects occur almost exclusively near the center of the convection cell. We characterized such events away from sidewalls in two ways. First we took the difference between two images, one showing an SV event like Figs. 19(a) and 19(d), and another without the SV distortion taken $9\tau_v$ earlier. The difference images corresponding to Figs. 19(a) and 19(d) are shown in Figs. 19(b) and 19(e). The area that is influenced by distortions from the SV event is readily determined. It is shown as a function of time as solid circles in Fig. 20, where it can be seen to grow essentially linearly with time. The second characterization was a measurement of the distance between the two defects generated by the SV event as a function of time. This was done by demodulating the Fourier transform so as to remove the mode with the dominant wave vector from both the image with the defect pair and the reference image taken earlier when there was no distortion from the SV event. The demodulated transforms still showed considerable structure due to the overall roll curvature. Nevertheless, the ratio of the moduli of these two demodulated transforms gave a sharp determination of the defect-core location, as shown by Figs. 19(c) and 19(f). The distance between the cores is easily measured, and is also plotted in Fig. 20.

With rotation, dislocation nucleations were concentrated at the sidewall and became much less frequent in the interior. In Fig. 21, we show a time sequence of images that illus-

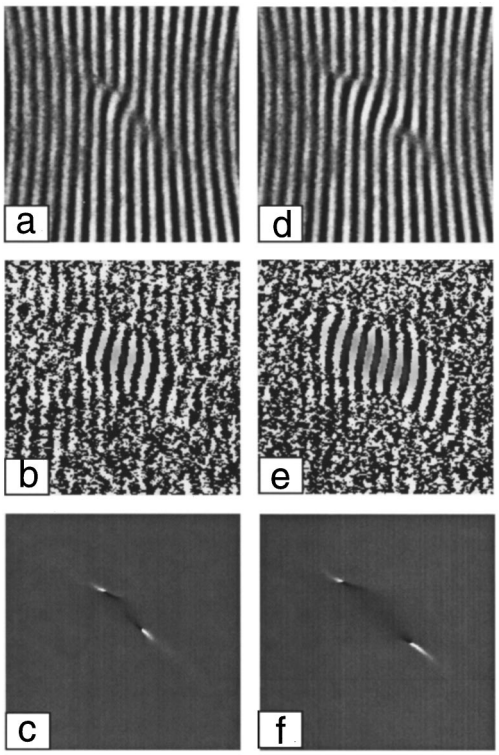

FIG. 19. Images (a) and (d) are for $\Omega=0$, $\epsilon=0.11$. They are separated in time by 1.8 τ_v. The differences between a reference image taken $9\tau_v$ before (a) and images (a) and (d) are shown in (b) and (e), respectively. Complex demodulation of images (a) and (d) normalized by the complex-demodulated reference image are shown in (c) and (f), respectively.

trates the nucleation of a dislocation defect near the wall by a complicated process that increases the local wave number. Also shown starting on the far right-hand edge is the appearance of an extra roll via an Eckhaus-like instability that increases the local wave number.

C. Pattern rotation and dislocation-defect motion

In variational systems, dislocation defects move primarily by climbing along the roll direction as opposed to gliding

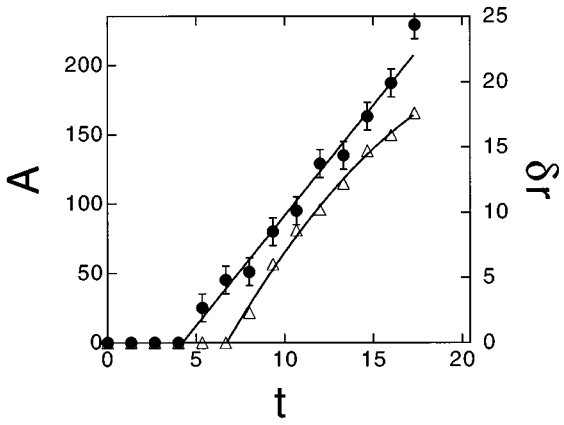

FIG. 20. Roll-distortion area and dislocation-defect separation as a function of time for $\Omega=0$, $\epsilon=0.11$. The left axis corresponds to data for the distortion area (●) and the right axis to the distance between dislocation defects (△).

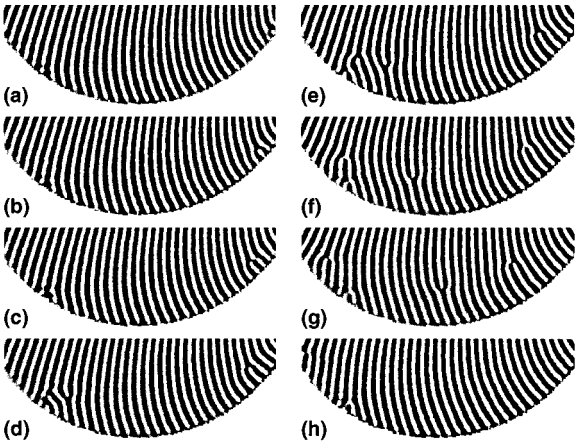

FIG. 21. Formation of defects at the side wall for $\epsilon=0.13$ and $\Omega=3.9$. The images are $40\tau_v$ apart. Two defects traveling in opposite directions merged between (g) and (h).

along the wave-vector direction [46]. In nonvariational systems such as low-σ convection and/or rotating convection, gliding motion can occur. A recent observation [58,67] in large-σ GSH and Boussinesq-convection simulations of rotating convection was that dislocation motion in rotating convection for large σ occurred mostly by glide motion, that rotation picked a preferential direction for that motion, and that the defects provided a mechanism for overall pattern rotation. In our system, dislocation defects were observed in many of the regions in Ω-ϵ parameter space. They are, however, clearly delineated from other dynamics only in region II. Much of our work on dislocation-defect motion in this region will be presented elsewhere [80] but here we include a summary of the observed behavior. We address two topics raised in simulations, namely, the net rotation of the mean wave-vector direction and the selection of a unique propagation direction for isolated defects.

One very noticeable feature of the SS patterns in region II is that their mean wave-vector direction rotates. Simulations yielded a rotation rate of the overall pattern that was proportional to Ω and suggested that gliding defects were responsible for this rigid rotation [67]. We measured the pattern rotation rate for several values of Ω. Our results for the pattern rotation rate ω in units of milliradians per τ_v are plotted versus ϵ in Fig. 22. (We chose to use the vertical diffusion time τ_v for the time scale although it is not obvious that it is relevant.) By interpolating these data, the variation of ω as a function of Ω is obtained as shown in Fig. 23. A corresponding calculation based on numerical simulations would be interesting for comparison.

The other very visible effect of rotation on the motions of dislocations throughout the cell but especially noticeable in the interior was that their direction of propagation was determined by the direction of rotation. In Fig. 24, a pattern is shown with several dislocations and the paths of those dislocations. For this case, the rotation vector $\vec{\Omega}$ is out of (clockwise) the plane of the image. We define a vector $\vec{b}$, which is parallel locally to the convection rolls. The direction of $\vec{b}$ is along the extra roll of the dislocation towards the singularity as illustrated in Fig 24. Another way to describe the dislocation is by its topological charge

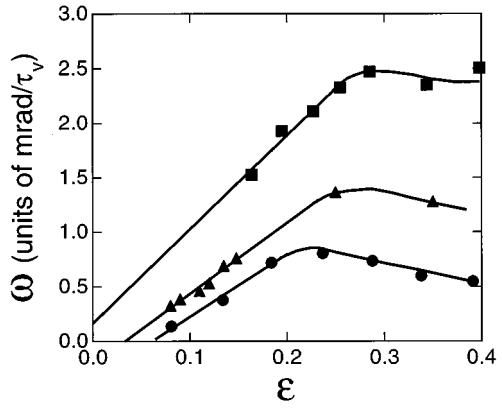

FIG. 22. Pattern rotation frequency ω vs ϵ for $\Omega=3.9$ (circles), $\Omega=6.6$ (triangles), and $\Omega=8.8$ (squares). The solid lines are guides to the eye.

$n=1/2\pi\oint_{\text{defect(cw)}}d\Theta$, where Θ is the phase of the complex convection roll amplitude with wave number k. We use the vector $\vec{b}$ instead of deriving a direction from n because the former is clearer and yields an unambiguous direction. The direction of the glide-velocity vector (the component of velocity along the local $\vec{k}$) is then given by the direction of $\vec{\Omega}\times\vec{b}$. We did not see any dislocations that violated this propagation direction for the rotation rates we investigated, $\Omega>3.9$. Overall the motion of defects was complicated with a variety of speeds and relative ratios of climb and glide that depended on the local pattern texture and the distance of the dislocations from the sidewalls. A systematic study of the effects of rotation on dislocation motion in straight-roll patterns similar to those done without rotation [81] would be extremely valuable.

V. CHARACTERIZATIONS OF AVERAGE QUANTITIES

The pattern textures and their spatiotemporal dynamics can be characterized to some extent by averages over many images of suitably defined parameters. The properties that we extracted from the images by either Fourier techniques or specialized algorithms as discussed in Ref. [54] are the average wave number $\langle k\rangle$, the correlation length ξ, the roll curvature γ, and the sidewall obliqueness β. The roll curvature and sidewall obliqueness are useful for small $\Omega\lesssim 8$ (regions I, II, and III) but yield little information about cellular patterns at higher Ω (regions IV, V, and VI). The correlation length provides some insight into the intermediate regions and the transition to the KL state. Finally, the average wave number is useful for high Ω where several regimes of linear dependence on ϵ were observed. We consider these quantities in order of their utility for increasing Ω.

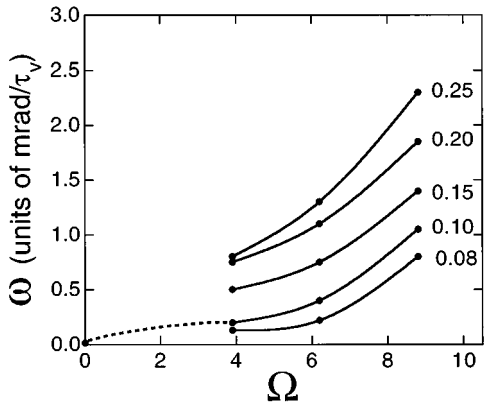

FIG. 23. ω vs Ω interpolated from data in Fig. 22. Values of ϵ are given in the figure. The solid and dashed lines are guides to the eye. The dashed line indicates less certainty in the interpolation.

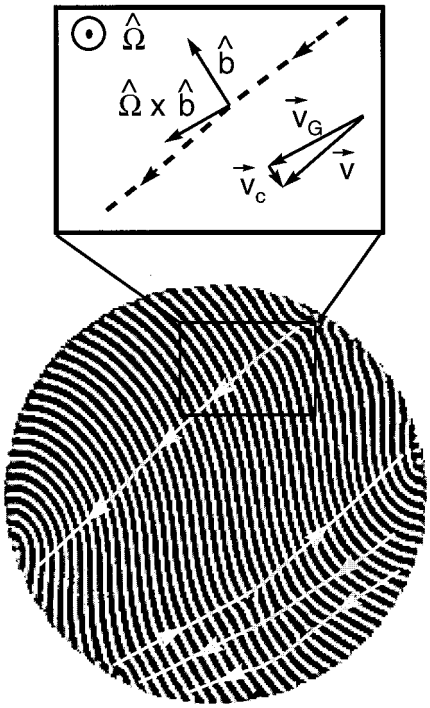

FIG. 24. Trajectory of some defects at $\Omega=6.2$ and $\epsilon=0.13$. The box in the image is expanded above to show details of the unit vectors describing the directions of the dislocation $\hat{b}$, of rotation about a vertical axis $\hat{\Omega}$, and of the glide direction of the dislocation $\hat{\Omega}\times\hat{b}$. Also shown is the decomposition of the dislocation velocity vector $\vec{v}$ into glide and climb components. Note that by definition the glide direction is along the local wave-vector direction.

A. Roll curvature and sidewall obliqueness

The average curvatures are plotted in Fig. 25(a). For $\Omega=0$, the main features of the data are an increase of $\gamma_{s,t}$ at about $\epsilon=0.1$, which reflects the appearance of sidewall foci, the relatively flat region $0.1<\epsilon<0.5$, and the large increase beyond $\epsilon\approx 0.55$, which is related to the onset of SDC [53,54]. The data with rotation do not show an increase for small ϵ but do have the flat dependence at intermediate ϵ and the rise that indicates the SDC state. Another way to consider these data is to construct contours of $\gamma_{s,t}$ as a function of Ω at fixed ϵ, determined from the data in Fig. 25(a) and shown in Fig. 26. The accumulation of defects near the sidewall contributed significantly to $\gamma_{s,t}$ at $\Omega=0$ and resulted in values comparable to those at $\Omega=8.8$ for $\epsilon\lesssim 0.4$. These sidewall defect clusters were much smaller and appeared less often for $\Omega>0$. On the other hand, the increase in $\gamma_{s,t}$ for $4<\Omega<9$ and $0.1\lesssim\epsilon\lesssim 0.4$ was caused by the SS distortion

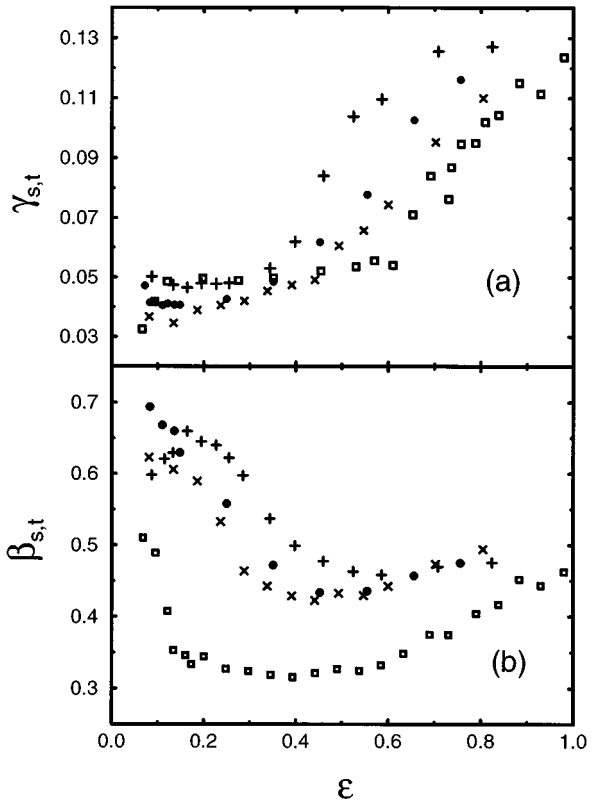

FIG. 25. (a) Average curvature $\gamma_{s,t}$ and (b) average sidewall obliqueness $\beta_{s,t}$ vs ϵ for $\Omega = 0$ (□), 3.9 (×), 6.2 (●), and 8.8 (+).

of the rolls taking on the ''S'' shape as seen in Figs. 9 and 10. The depressed onset for SDC as a function of Ω was responsible for the larger $\gamma_{s,t}$ at higher Ω for $0.4<\epsilon<1$. Whereas the SDC onset was $\epsilon\approx 0.55$ for zero rotation, it decreased to almost 0.5 for $\Omega=3.9$ and 0.4 for $\Omega=6.2$. The slopes of $\gamma_{s,t}$ as a function of ϵ after the onset of SDC were approximately independent of Ω as seen in Fig. 25, even though the size of the spirals decreased for larger Ω. This is surprising at first glance because, averaged over a single spiral, the curvature would be larger for a small spiral than for a large one and, additionally, small spirals could be packed

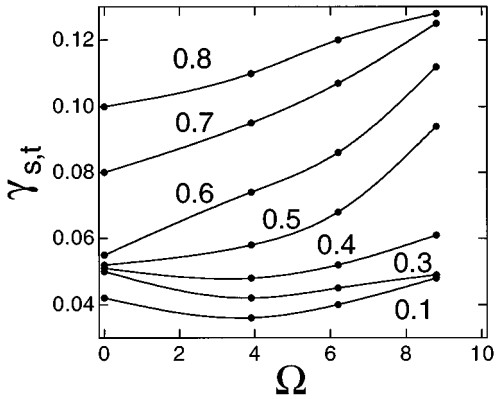

FIG. 26. Average curvature $\gamma_{s,t}$ vs Ω for the values of ϵ indicated in the figure interpolated from data in Fig. 25(a). Solid lines are guides to the eye.

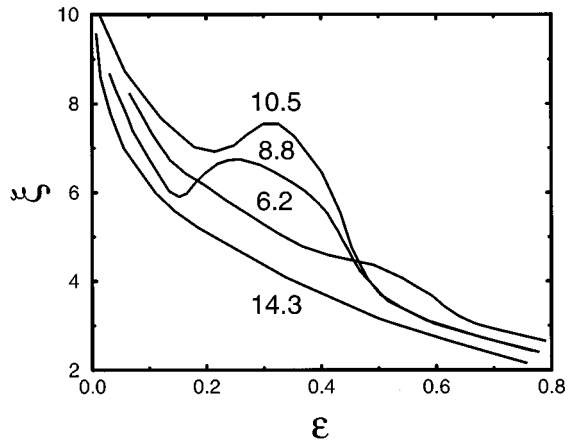

FIG. 27. Correlation length ξ vs ϵ for the values of Ω indicated in the figure. The data were smoothed slightly.

more densely than large ones. These factors were offset, however, by the straighter rolls between the spirals and the more angular appearance of the spirals at larger rotation rate, so the average curvature at the same distance from the SDC onset remained approximately independent of Ω.

The sidewall obliqueness data are presented in Fig. 25(b). Unlike the curvature, the obliqueness at $\Omega=0$ was always smaller than that at the same ϵ under rotation. Below the onset of SDC, this is so because the rolls of the SS pattern end less perpendicular to the wall for $\Omega>0$. Above the onset, the smaller $\beta_{s,t}$ was due to a decrease of the size of sidewall foci with increasing Ω. For $\Omega=8.8$ and $\epsilon\lesssim 0.2$, $\beta_{s,t}$ was smaller than at $\Omega=6.2$. The appearance of KL fronts at the sidewall caused rolls to be more perpendicular to the sidewall, so $\beta_{s,t}$ was smaller. At larger ϵ where KL fronts were rarely observed, $\beta_{s,t}$ became larger again because of the increased curvature of the ''S''-shaped patterns.

B. Correlation length

The average correlation length ξ calculated from the structure factor of pattern sequences has been shown to provide a simple, well-defined measure of the spatial order of these sequences [27,47,54,61]. Previously, we used the correlation-length analysis to determine spatial scaling in the Küppers-Lortz regime (region V) at small $\epsilon<0.2$ [27]. Here we apply it also to aid in the characterization of pattern order in regions II and III where weak rotation effects are seen. In Fig. 27, ξ is shown as a function of ϵ. Generally ξ decreases with ϵ with the exception of the bumps in the range $0.2<\epsilon<0.5$ for $\Omega=$ 8.8 and 10.5. For higher and lower Ω, ξ decreases monotonically with ϵ. The bumps are well correlated with the development of the SS distortion seen in region II of Fig. 7. More insight is obtained by plotting contours of ξ as a function of Ω, as shown in Fig. 28 where the data were interpolated from data in Figs. 27 and 29. At fixed $0.2\lesssim\epsilon\lesssim 0.5$ and for $\Omega<10$, ξ initially increases with Ω consistent with an increased ordering resulting from the development of the S shape. Above $\Omega\approx 12$ for that same ϵ range, ξ falls quickly, indicating the transition to the cellular regime generated by the Küppers-Lortz instability.

For $\Omega=0$, the dependence of ξ on ϵ was first studied by Morris *et al.* [47] who showed that a power-law scaling of

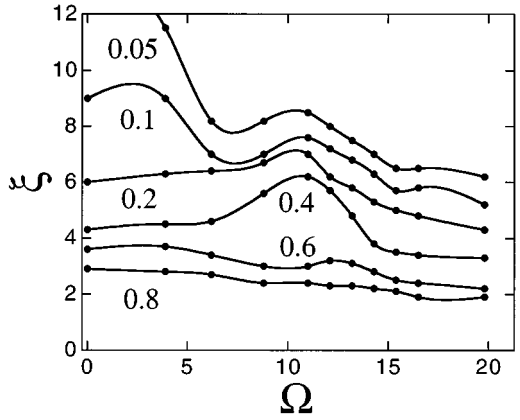

FIG. 28. Correlation length ξ vs Ω for values of ϵ as indicated. Data were interpolated from data at fixed Ω. Solid lines are guides to the eye.

the form $\xi \propto \epsilon^{-x}$ with $x=-1/2$ was consistent with their data over roughly a decade in ϵ between 0.1 and 1. Our measurements [27] for $\Omega>0$ showed an exponent value between 0.20 and 0.25 in region V. In Fig. 29, we show data on log-log scales for three values of Ω and for values of ϵ that span regions V and VI. The data for the different rotation rates fall roughly on parallel curves in each of two distinct regimes. For $\epsilon \lesssim 0.1$ they show again the small exponent reported earlier. However, for $0.3 \lesssim \epsilon \lesssim 1$ the slopes given by the data are consistent with an effective exponent of about 3/4. This latter result is larger than the $\Omega=0$ exponent [47] but smaller than the exponents of between 1 and 3/2 suggested recently by GSH simulations for $\sigma=2$ and $\Omega=22$ and 28 [23]. The two separate effective scaling ranges are intriguing, but their origin is completely unclear. On the basis of the general structure of Ginzburg-Landau equations an exponent value of 1/2 might have been expected close to onset. For ϵ of order 1, we do not know of any prediction.

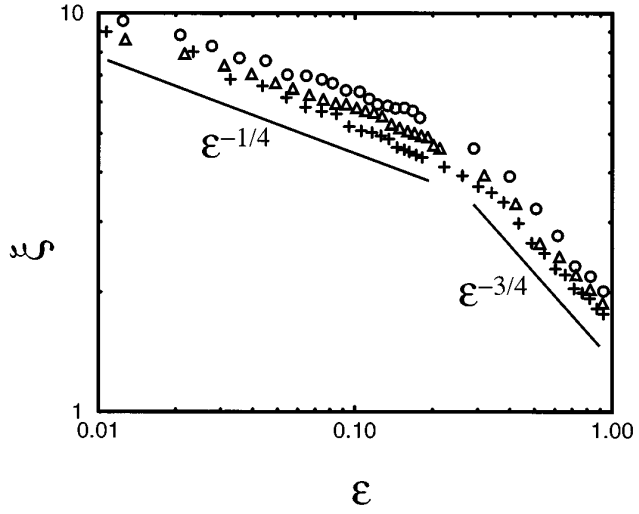

FIG. 29. Log-log plot of correlation length ξ vs ϵ for $\Omega=14.3$ ($\bigcirc$), $\Omega=16.5$ ($\triangle$) and $\Omega=19.8$ ($+$). For comparison, the solid lines indicate power-law behavior with exponents of 1/4 and 3/4.

C. Average wave number

The average wave number $\langle k \rangle$ is a reflection of the different wave-number-selection processes that compete in a complicated textured pattern. Only in very ordered patterns such as an axisymmetric one of concentric rolls is the wave-number-selection process unique. In previous studies without rotation, we considered the wave-number selection for axisymmetric patterns [50] and the more complex situation for textured patterns [54]. In textured patterns there is a distribution of wave numbers that can be partially characterized by $\langle k \rangle$, with $\langle k \rangle$ still uniquely selected by the prevailing textures. One interesting feature of the selection at small ϵ for $\Gamma=40$ was that the wave number initially increased before turning back towards low wave number for $\epsilon \gtrsim 0.1$. We now consider the effects of rotation on the behavior of the average wave number. The wave numbers $k_c(\Omega)$ at onset determined by linear extrapolation of $\langle k \rangle$ for small ϵ to $\epsilon=0$ were presented in Sec. III.

The variation of $\langle k \rangle$ with ϵ is shown in Fig. 30(a) for $\Omega=0$, 3.9, 6.2, and 8.8. The feature of increasing wave number at small ϵ is maintained in the presence of rotation except for $\Omega=8.8$ where there is an initial decrease followed at $\epsilon \approx 0.1$ by an increase in $\langle k \rangle$ and finally a decreasing wave number for $\epsilon \gtrsim 0.2$. For $\Omega=0$, 3.9, and 6.2, the variation of $\langle k \rangle$ is about the same for $\epsilon \lesssim 0.30$, at which point the data for $\Omega=6.2$ break off and move more quickly to lower k. Similarly, at $\epsilon \approx 0.45$ the data for 3.9 move sharply to lower k. This trend towards lower wave number is consistent with the appearance of the SDC state and is also reflected in the roll curvature [Fig. 25(a)]. At higher ϵ and after the jump to lower k, the slope of $\langle k \rangle$ becomes steeper, indicative of well-developed SDC [54]. The behavior for $\Omega=8.8$ is probably caused by KL dynamics in region IV beginning to influence wave-number selection for small ϵ, followed by dislocation processes winning out for a small interval of ϵ, and finally the SDC state coming in a little higher. Multiple influences are clearly at work here near the borders of several of the regions of parameter space shown in Fig. 7.

The behavior of $\langle k \rangle$ at higher Ω is quite different from that for $\Omega \lesssim 9$. Figure 30(b) shows $\langle k \rangle$ as a function of ϵ for $\Omega=10.5, 15.4$, and 19.8. Common to all three data sets are the two linear sections, one near the onset and the other for $\epsilon \gtrsim 0.5$. The straight lines in Fig. 30(b) are fits to the two linear sections, and they highlight the differences among the plots, namely, the rounding at the transitional region from low to high ϵ. The origin of the linear sections and the rounding is unclear, but their properties show a systematic dependence on Ω. At $\Omega=10.5$, $\langle k \rangle$ deviated from its linear behavior near onset for $\epsilon \approx 0.15$; it resumed its linear dependence on ϵ at $\epsilon \approx 0.45$ with a different slope. Over a large range of ϵ, the values of $\langle k \rangle$ were larger than extrapolations based on either of the two linear regions. This rounding of the transition between the two sections decreased as Ω increased. At $\Omega=19.8$, there was essentially no rounding, and $\langle k \rangle$ varied linearly with ϵ but with two different slopes, one for $\epsilon \lesssim 0.36$ and another for $\epsilon \gtrsim 0.36$. In Fig. 30(b), the quantities ϵ_1 and ϵ_2 are the points at which $\langle k \rangle$ deviated from the linear fits for small and large ϵ, respectively. The changes of ϵ_1 and ϵ_2 with Ω are summarized in Fig. 31(a). Whereas

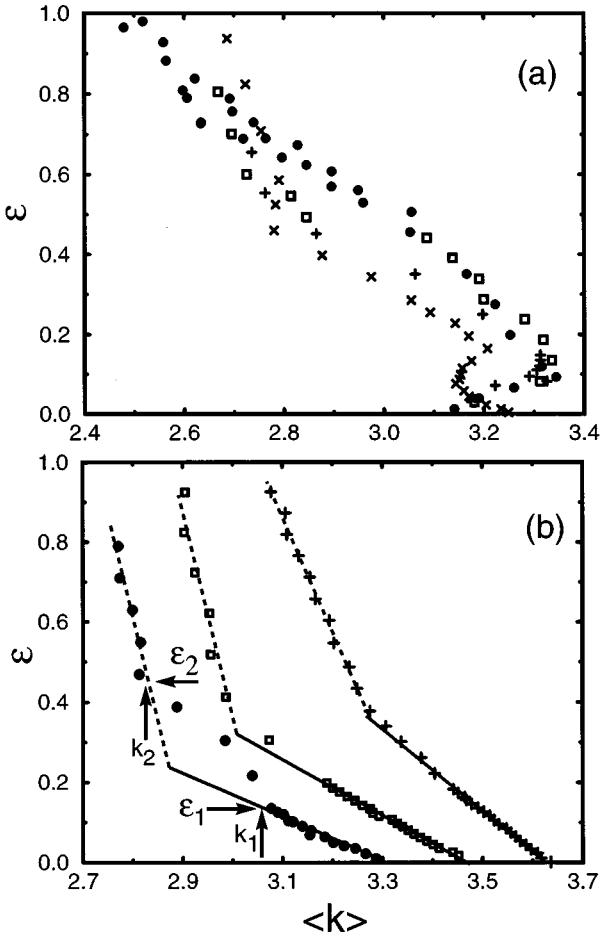

FIG. 30. Plots of $\langle k \rangle$ vs ϵ for (a) $\Omega = 0$ (●),3.9 (□), 6.2 (+), and 8.8 (×), and (b) $\Omega = 10.5$ (●),15.4 (□), and 19.8 (+). The solid and dashed straight lines are fits to data at low and high ϵ respectively. The definitions of k_1, k_2, ϵ_1, and ϵ_2 are illustrated for $\Omega = 10.5$.

ϵ_2 did not vary in a simple way, ϵ_1 increased linearly with Ω.

The values of $\langle k \rangle$ at the end points of the linear regions, ϵ_1 and ϵ_2, are denoted as k_1 and k_2, respectively, and illustrated in Fig. 30(b). As can be seen in Fig. 31(b), the values of k_2 were all smaller than k_1, and the difference between k_1 and k_2 decreased with increasing Ω. The slopes $d\langle k \rangle / d\epsilon$ from the fits, plotted in Fig. 32, are negative, reflecting the wave-number decrease with ϵ. The slope at large ϵ did not vary much with Ω, but near onset it varied considerably.

The problem of wave-number selection for concentric patterns and $\Omega > 0$ was also studied, but in a $\Gamma = 41$ cell with a ''spoiler tab.'' Details of the construction and the concentric-pattern dynamics at $\Omega = 0$ are contained in Ref. [50]. As shown in Fig. 33(a), the pattern consisted of axisymmetric rolls coexisting with an annular cross-roll state confined near the sidewall. At $\Omega = 0$, this state was the preferred pattern above onset and remained stable for $\epsilon \leqslant 0.08$. Under rotation, the wave number changed, as seen in a comparison between Figs. 33(a) and 33(b), but the pattern still remained stable for $\epsilon \leqslant 0.08$ and $\Omega \leqslant 9.5$. For $\Omega > 9.5$, the pattern could not be maintained at any ϵ as the cross rolls

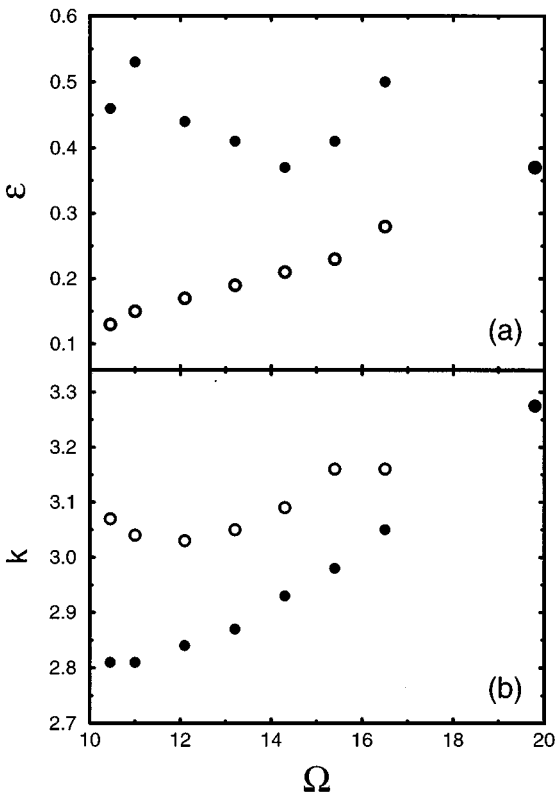

FIG. 31. (a) Plots of ϵ_1 (○), ϵ_2 (●) and (b) k_1 (○), k_2 (●).

grew into the axisymmetric rolls in a manner similar to sidewall-initiated KL fronts. The destruction of the concentric pattern left a textured pattern similar to the ones in region IV as in Fig. 13. The experiments were conducted by ramping Ω at constant $\epsilon = 0.025$ from 0 to 9.5 and then back down to 0 in steps of 0.25. The measured wave number is presented in Fig. 34 together with the theoretical curve for k_c for comparison. The length of the cross rolls changed to accommodate smooth increases or decreases of the wavelength of the axisymmetric rolls. The large changes in $\langle k \rangle$ came from a reversal in the fluid flow direction at the umbilicus that accompanied a creation or destruction of one roll. Hysteresis in the selected wave number as a function of Ω

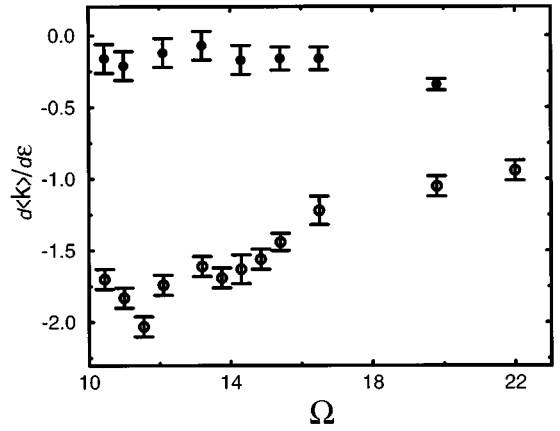

FIG. 32. Plots of $d\langle k \rangle / d\epsilon$ vs Ω, near onset (○) and for high ϵ (●).

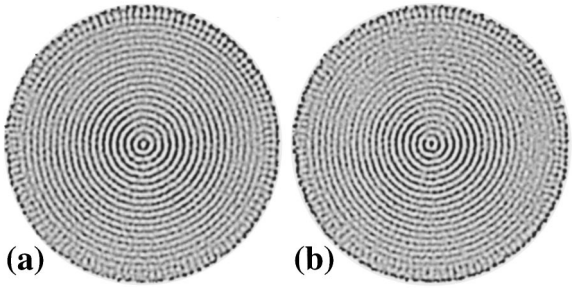

FIG. 33. Concentric patterns in a $\Gamma=41$ cell at $\epsilon\approx 0.03$: (a) $\Omega=0$ and (b) $\Omega=6.25$.

occurred at $\Omega\approx 4$ and $\Omega\approx 7$. This is similar to the behavior of concentric patterns in water without rotation [82] where hysteresis was observed as ϵ changed. The hysteresis here is unusual as $\langle k\rangle$ remained close to 3.2 over a wider range in Ω during ramping up than ramping down as seen in Fig. 34. The cause of this behavior is unclear.

VI. PATTERN DYNAMICS

The textures and averaged properties of patterns presented in previous sections are the result of complicated pattern dynamics. In this section, we present pattern sequences that illustrate the dynamics in the regions labeled in the parameter-space diagram of Fig. 7. The richness of the dynamics needs to be condensed for presentation here and we have no doubt omitted or missed altogether interesting processes that might be important. Nevertheless, the sequences presented do reflect the most obvious characteristics of the separate regions.

A. Region II: S-shaped patterns and dislocation motion

The dynamics of patterns in region II involved primarily dislocation-defect motion within the generally S-shaped pattern. The defect nucleation could be divided into bulk nucleation, identifiable with the SV instability, and sidewall nucleations of dislocations. At $\Omega=0$, the roll pinching typical of SV usually took place near the central region of the cell, but under rotation, more of the roll pinchings occurred near sidewall foci. This is illustrated by the time series of images

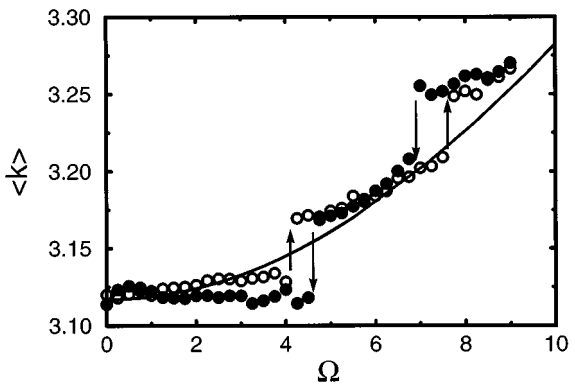

FIG. 34. The mean wave number $\langle k\rangle$ of concentric patterns at $\epsilon=0.025$ for increasing (○) and decreasing Ω (●). The solid line shows k_c from linear stability analysis for comparison.

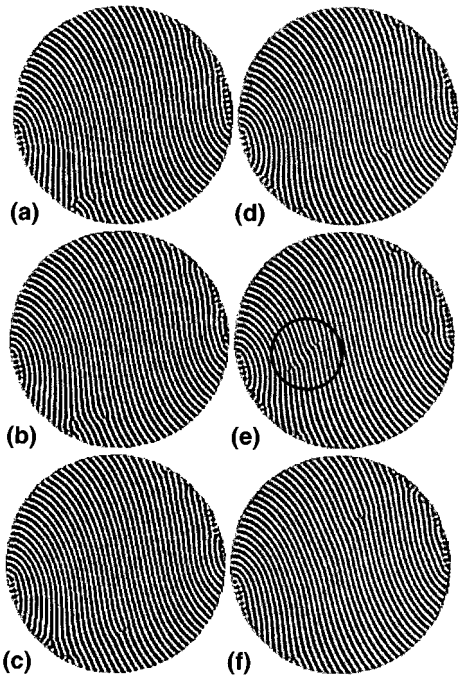

FIG. 35. Time sequence showing defect motion and the skewed-varicose instability at $\epsilon=0.13$ and $\Omega=3.9$ in region II. The circle in (e) encloses a pair of skewed-varicose-generated defects. The images are $40\tau_v$ apart.

taken $40\tau_v$ apart at $\epsilon=0.13$ for $\Omega=3.9$ shown in Fig. 35. A pair of defects was generated when roll pinching occurred near a wall defect at the lower left side of Fig. 35(a). One of the defects glided across the rolls while climbing along the rolls toward the central region of the cell. It eventually merged with the cross-roll patch at the right side of the cell. The other traveled in the opposite direction along the sidewall and merged with the left cross-roll patch. The motion of the defects was mainly across the rolls (gliding) with less movement along the roll axes (climbing). This is seen in the path of the right-traveling defects, which moved across almost the entire width of the cell while climbing less than half the cell width. This is similar to results from a numerical simulation for $\sigma=\infty$ where the defect motion was found to be mostly gliding rather than climbing [83]. In Fig. 35(a), the lower-left sidewall-defect structure near which the roll-pinching occurred was pinned and remained immobile throughout this sample image sequence, but at other times such structures could move and merge with the cross-roll patch. Figure 35(e) contains an infrequent SV defect-pair creation away from the sidewall, an event resembling occurrences at $\Omega=0$. While the defects were formed and subsequently propagated toward the cross rolls, the underlying straight-roll pattern gradually rotated in the direction of rotation. This change in roll orientation was smooth and did not involve discrete large jumps as would be expected from the KL instability.

At higher Ω in region II, the rolls were much more curved and the S shape was accentuated. Many defects were present simultaneously but, unlike at $\Omega=3.9$, defects did not accumulate near the sidewall as in Fig. 9. This time dependence was captured in the image sequence, Fig. 36, taken at $\epsilon=0.23$ and $\Omega=8.8$, spaced $20\tau_v$ apart. Whereas the nucle-

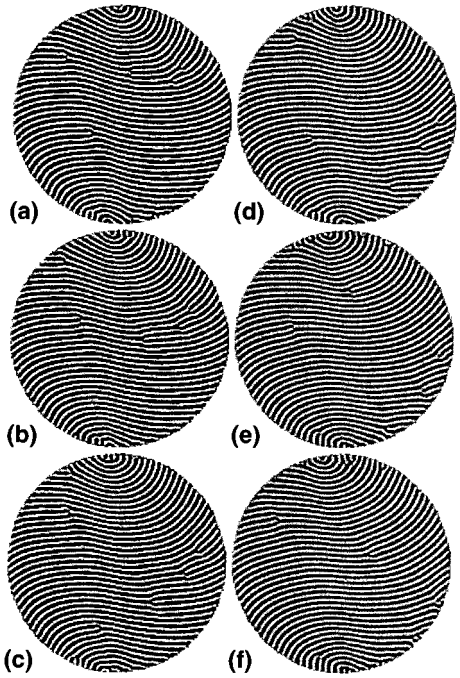

FIG. 36. Time sequence showing defect motion at $\epsilon \approx 0.23$ and $\Omega = 8.8$ in region II. The images are $20\tau_v$ apart.

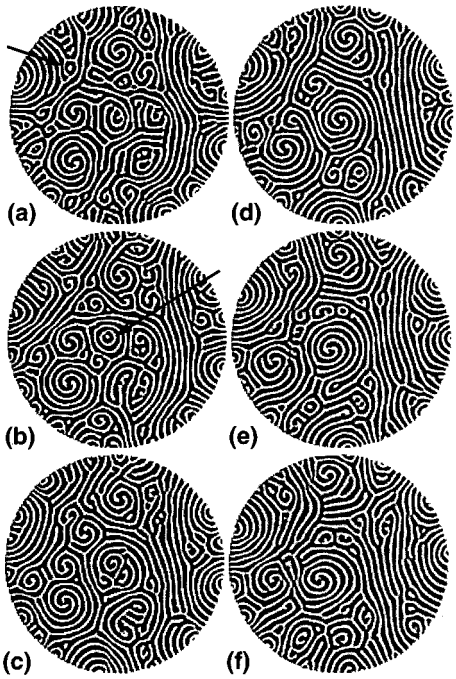

FIG. 37. Time sequence of spiral-defect chaos at $\epsilon \approx 0.81$ and $\Omega = 3.9$ in region III. The images are $40\tau_v$ apart. Arrows in (a) and (b) point to target defects that evolve into spiral defects.

ation of defects took only about $3-5\tau_v$, the defect movement was slow enough that individual defects can be followed in this sequence. The defects traveled according to their topological charge as discussed earlier. The orientation of the underlying roll pattern still advanced slowly in the direction of rotation, as expected from similar observations at smaller Ω. Infrequent KL fronts were also initiated by defects at the sidewall. They rarely propagated across the whole cell and only affected a portion of the pattern.

B. Regions III and VI: Spiral-defect chaos

The existence of spiral and target defects was characteristic of region III. At low $\Omega = 3.9$, target defects first appeared near $\epsilon = 0.45$. They sometimes evolved into spirals, and the number and sizes of the spirals fluctuated in time, similar to the case for $\Omega = 0$. At $\epsilon \approx 0.7$ spirals were always present, but most spirals with diameter larger than $7-8d$ were two-armed. Smaller spirals generally evolved from target defects or dislocations and were usually one-armed. The dynamics were quite fast with continuous creations and destructions of spirals, but the images in Fig. 37 taken $40\tau_v$ apart at $\epsilon = 0.81$ captured the evolution of several structures in detail. The arrow in Fig. 37(b) points to a three-ring target that grew from a small spiral and then became a spiral again in Fig. 37(c). The spiral then merged with surrounding spirals to form a large two-armed spiral, about $14d$ in diameter, in Fig. 37(d). This large spiral was subsequently destroyed when it moved left toward the wall several time steps later. The change of a target defect into a small spiral is also visible in these images as seen in a comparison between Fig. 37(a) and Fig. 37(b) of the defect indicated by the arrow in Fig. 37(a).

At $\epsilon \approx 0.3$ sidewall-defect clusters nucleated small target defects, which stayed within $10d$ and $12d$ of the sidewall, and at $\epsilon \approx 0.4$, these target defects sometimes evolved into small spirals. The patterns then resembled those at $\epsilon \approx 0.5$ and $\Omega = 0$; an image sequence taken at $\epsilon = 0.40$ illustrating the creation and annihilation of small spirals is shown in Fig. 38. At even higher ϵ, recognizable spirals appeared more often, and the average number of spirals increased. Large spirals appeared infrequently, as seen in Fig. 39, which is an image sequence at $\epsilon = 0.59$ spaced $6.7\tau_v$ apart. Most spirals measured $6-8d$ in diameter and were smaller than typical spirals at smaller Ω. The spirals were more angular as illustrated by the large double-armed spiral indicated by the arrow in Fig. 39(d). The average lifetime of a spiral was quite short, about $20\tau_v$. The short duration is typified by the small spiral, indicated in Fig. 39(a), which was nucleated and destroyed in less than $20\tau_v$. Away from the spirals, the rolls joined in a more angular fashion. This rather angular feature of the rolls was reminiscent of the discrete orientation change caused by the KL instability despite the almost complete absence of KL fronts for $\epsilon \gtrsim 0.2$. A final interesting phenomenon seen in some images in this region, several white cells in a row, is shown by the arrows in Figs. 39(f) and 40(a). This pattern may be an indication of local cross-roll instability.

For progressively higher Ω in region III, spirals become smaller and less frequent. The last remnants of discernible spiral activity was for $\Omega = 12.1$. In Fig. 40, for $\epsilon = 0.37$ and $\Omega = 12.1$, a time sequence of images shows several small spirals and some clustered curved defects. Also noticeable are lines of cells that are similar to the cross-roll nucleations seen at higher σ and $\Omega = 0$ [84]. These cross rolls sometimes disappeared without affecting the texture, much as typified by the ones indicated by the left arrow in Fig. 40(a). Some-

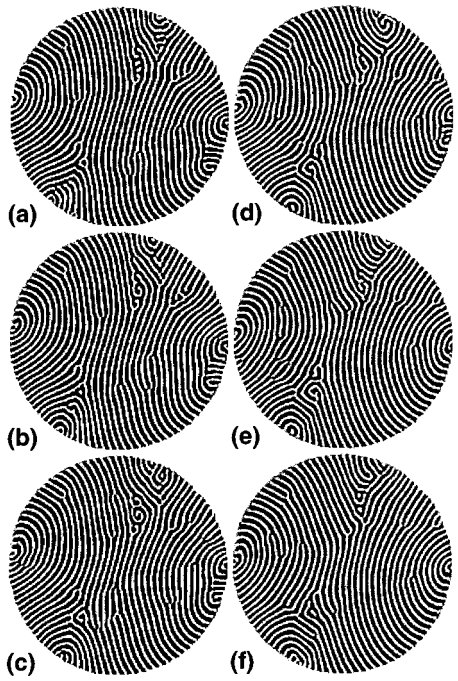

FIG. 38. Time sequence of spiral-defect chaos at $\epsilon \approx 0.40$ and $\Omega = 8.8$ in region III. The images are $13.3\tau_v$ apart.

times spirals would arise from these cross rolls as shown by the right arrow in Fig. 40.

At $\epsilon \approx 0.5$, where SDC was observed at lower Ω, the patterns consisted of many target defects and some small spirals measuring $4-5d$ in diameter. No spiral larger than $6d$ in diameter was seen. A time series of images spaced $6.7\tau_v$ apart, taken at $\epsilon = 0.55$, is shown in Fig. 41. The dynamics was faster than captured by this sequence, but typical features can be seen in the figure. The target defects were quite mobile and occasionally annihilated each other by collision.

For higher $\Omega > 12.1$, the dynamics were complicated, consisting of many defects and cellular patches, and are impossible to represent clearly with still images. Clearly identifi-

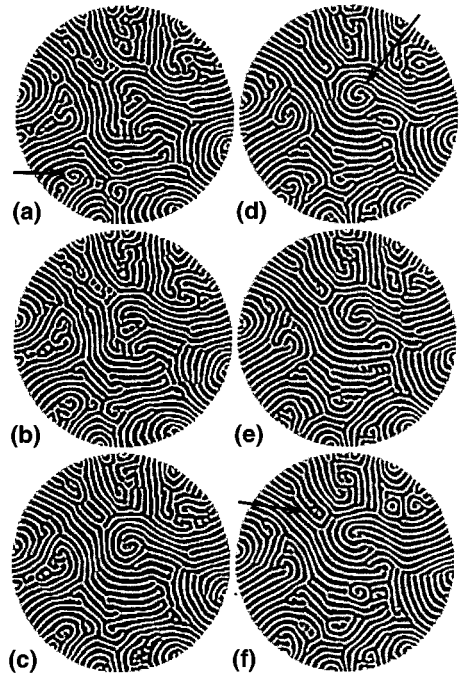

FIG. 39. Time sequence of spiral-defect chaos at $\epsilon \approx 0.59$ and $\Omega = 8.8$ in region III. The images are $6.7\tau_v$ apart. Arrows point to (a) single-arm spiral, (d) double-arm spiral, and (f) localized cross rolls.

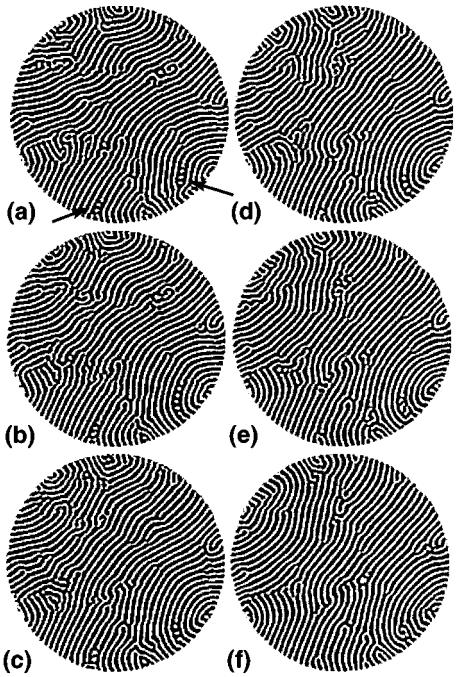

FIG. 40. Time sequence at $\epsilon \approx 0.37$ and $\Omega = 12.1$ in region VI. The images are $6.7\tau_v$ apart. The arrows point to two cross roll regions.

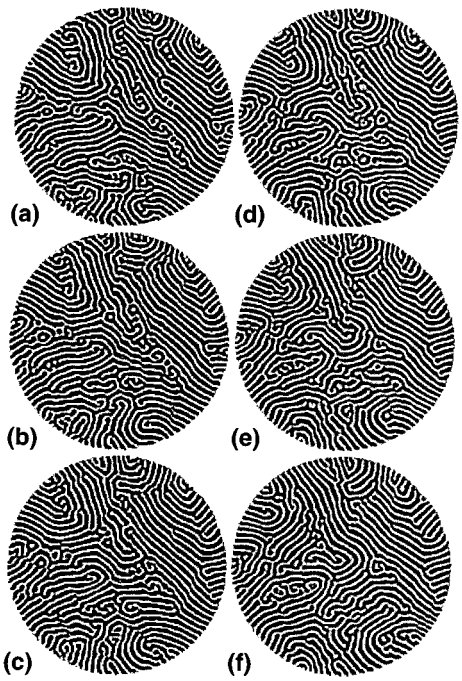

FIG. 41. Time sequence at $\epsilon \approx 0.55$ and $\Omega = 12.1$ in region VI. The images are $6.7\tau_v$ apart.

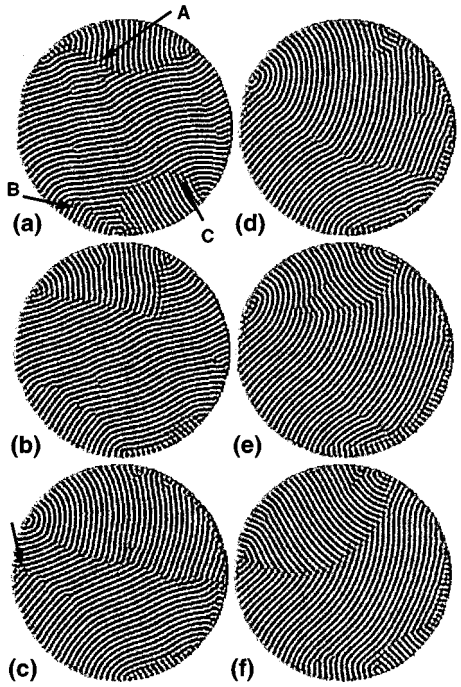

FIG. 42. Time sequence of Küppers-Lortz fronts mixed with dislocation defects at $\epsilon \approx 0.06$ and $\Omega = 8.8$ in region IV. The images are $40\tau_v$ apart. Arrows in (a) point to different KL fronts. The arrow in (c) shows the dissipated remains of KL front *B* indicated in (a).

able spirals were only observed rarely, but small highly curved defects were present at all times.

C. Region IV: Küppers-Lortz fronts

The Küppers-Lortz instability was not observed for $\Omega \lesssim 5$ up to $\epsilon \approx 1$ where spiral-defect chaos dominated. The first appearance of the KL instability was at $\Omega = 6.2$ and $\epsilon = 0.07$ where the main time dependence was associated with dislocation motion. By $\Omega = 8.8$, KL fronts occurred near the onset of convection and were responsible for much of the dynamics, as seen in Fig. 42, which was taken at $\epsilon = 0.06$. Three KL fronts, labeled *A*, *B*, and *C*, are visible in Fig. 42(a), and dislocation defects are seen in the region with nearly horizontal rolls. The horizontal rolls were unstable with respect to fronts *A* and *B* while the rolls marking front *C* were unstable to the horizontal rolls. As a result, fronts *A* and *B* propagated away from the wall and grew into the horizontal rolls, but front *C* moved toward the wall. In Fig. 42(b) front *C* had reached the wall, and front *B* had merged smoothly into the horizontal rolls. This smooth merging occurred frequently in KL front propagation for $\Omega \lesssim 12$; its main feature involved the growing rolls linking up with the decaying rolls, eventually forming smoothly curved continuous rolls. A line of defects separated the growing from the unstable rolls, as indicated by the arrow in Fig. 42(c), and the defects traveled left toward the wall leaving behind smoothly curved rolls as in Fig. 42(d). The same merging phenomenon also occurred at the end of large orientational changes as illustrated by front *A*, which was more well defined than front *B*. The angles between the growing rolls behind front *A* and the unstable rolls varied little from one end of the front to the other, as seen in Fig. 42(b). In Fig. 42(c), the left side of front *A* had disappeared, and the two sets of rolls had merged into curved rolls as sharp angles between the two sets of rolls disappeared. The remaining defects at the interface propagated toward the right, leaving behind slightly curved rolls, as seen in Fig. 42(d) and Fig. 42(e). Even with this smoothing process, the overall roll orientation still changed by discrete steps, but the changes varied between 30° and 70°. This is fundamentally different from the smooth angular changes observed at larger ϵ, which were caused by repeated dislocation-defect nucleations. Before front *A* had traversed the whole cell, another front was nucleated near the wall at the upper right side, and its progress is shown in Fig. 42(e) and Fig. 42(f).

D. Region V: Küppers-Lortz dynamics

For a spatially uniform straight-roll pattern at the onset of convection, theoretical calculations predicted the appearance of the KL instability at the critical rotation rate $\Omega_c \approx 13$ for our system [79]. The inclusion of the spatial dependence of the roll amplitude showed that KL fronts could propagate for $\Omega < \Omega_c$ provided such fronts exist [19]. The existence of grain boundaries near the sidewall resulted in the appearance of KL front propagation for $\Omega \gtrsim 6$, substantially below Ω_c. At $\Omega = 12.1$ and $\epsilon = 0.11$ the KL fronts initiated by the grain boundaries remained quite dominant in the dynamics, but the pattern was always composed of several domains of similarly oriented rolls with different roll orientations from patch to patch as in Fig. 43. In addition to fronts nucleated at the sidewall, occasionally new fronts appeared spontaneously in the interior of the cell. One such front is indicated by the arrow in Fig. 43. This spontaneous formation of new fronts was not observed for $\Omega \lesssim 11$. More details on region V are presented elsewhere [27,28].

VII. CONCLUSIONS

The experimental results presented in this paper fall into several categories: (1) the linear results for the onset Rayleigh number and the pattern wave number that agree quantitatively with theoretical predictions; (2) qualitative behavior of pattern dynamics that was consistent with theoretical expectations and numerical simulations; (3) new phenomena, both qualitative and quantitative, for which no theory has been developed so far. The qualitative behavior of patterns included observations about the form and frequency of the known long-wavelength instabilities. The skewed-varicose instability was chief among these and was responsible for much of the dynamics for small ϵ and Ω. The form of the SV instability under rotation was studied, and the SV angle as a function of Ω was determined. Dislocation defects and the S-shaped pattern dominated this region in which slow overall pattern rotations were observed. The precession frequencies for this slow rotation were determined. Key to understanding the results near onset was the important contribution of the sidewall, which served to nucleate both dislocation defects or Küppers-Lortz fronts, depending on Ω. This was explicitly illustrated by the different pattern dynamics near onset in cells with different Γ that had differences in spatial homogeneity. The other striking feature for

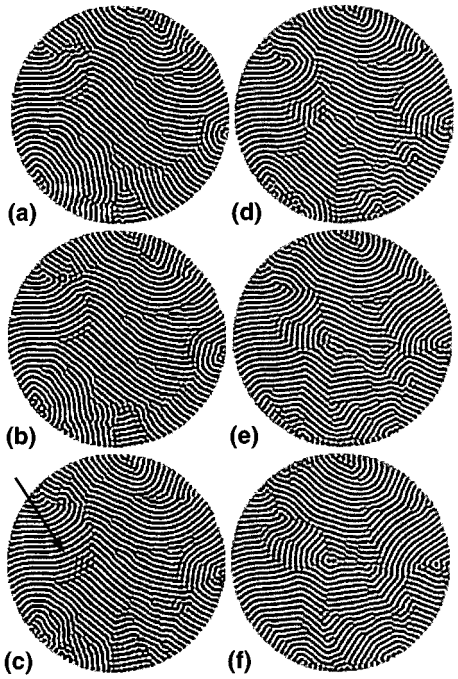

FIG. 43. Time sequence of Küppers-Lortz-unstable domains mixed with dislocation defects at $\epsilon \approx 0.11$ and $\Omega = 12.1$ in region V. The images are $8.9\tau_v$ apart. Arrow in (c) points to a region where a new domain nucleated away from the boundary can be seen in (d).

small Ω and ϵ was the strong polarizing effect of rotation on the direction of dislocation motion and the significant enhancement of glide motions for these defects.

A well-studied state for $\Omega = 0$ is the spiral-defect-chaos state. Under rotation, this state dominates for higher ϵ but undergoes a continual metamorphosis as Ω is increased until there are no spirals at all but a state of highly curved rolls reminiscent of the SDC state. The first appearance of spirals as a function of ϵ is also affected by rotation with smaller onset values of ϵ for larger Ω. This combination of SDC dynamics and rotation is complex and may be hard to untangle as it includes mean-drift, local defect structures, and Küppers-Lortz dynamics. It is certainly a complicated example of spatiotemporal chaos in two-dimensional patterns.

Several quantitative characterizations of wave-number selection and spatial correlations are not addressed by theory but may be amenable to theoretical analysis. The first is the scaling of the correlation length as a function of ϵ, which divides itself naturally into two regions, one near onset with a scaling exponent of about 1/4 and another at intermediate ϵ where the exponent is close to 3/4. The other very interesting quantitative feature of the data is the linear dependence of the average wave number near onset near and above the predicted critical Ω_c for the KL instability. Whereas the average wave number for smaller Ω fluctuates on long time scales, the faster dynamics and more cellular structure induced by the KL instability produces an average wave number that is very steady in time and has a very linear dependence on ϵ.

In summary, we have illustrated some of the richness that exists for rotating layers of fluid heated from below. We have observed local signatures of skewed-varicose, Eckhaus, and cross roll instabilities as well as the global Küppers-Lortz instability and the state of spiral-defect chaos. A thorough theoretical study of the stability boundaries as a function of Prandtl number and rotation rate would be very valuable. Numerical simulations of these states is another area that is just beginning and for which a wealth of comparisons could be made. We hope that our work will stimulate such investigations.

ACKNOWLEDGMENTS

We gratefully acknowledge support from a UC/LANL INCOR grant and from the U.S. Department of Energy. We thank Ning Li, Mike Cross, and Werner Pesch for useful discussions, Eberhard Bodenschatz, John de Bruyn, David S. Cannell, Stephen Morris, and Steve Trainoff for their contributions to the design of the apparatus, and Tom Clune and Edgar Knobloch for providing us with data on the linear stability boundary and on the Küppers-Lortz critical rotation rate.

[1] S. Chandrasekhar, *Hydrodynamic and Hydromagnetic Stability* (Oxford University Press, Oxford, 1961).
[2] G. Küppers and D. Lortz, J. Fluid Mech. **35**, 609 (1969).
[3] G. Küppers, Phys. Lett. **32A**, 7 (1970).
[4] R. M. Clever and F. H. Busse, J. Fluid Mech. **94**, 609 (1979).
[5] E. L. Koschmieder, Beitr. Phys. Atmos. **40**, 216 (1967).
[6] H. T. Rossby, J. Fluid Mech. **36**, 309 (1969).
[7] R. Krishnamurti, *Proceedings of the 8th Symposium on Naval Hydrodynamics* (Office of Naval Research, Washington, D.C., 1971), p. 289.
[8] K. E. Heikes, Ph.D. thesis, University of California, Los Angeles, 1979.
[9] F. H. Busse and K. E. Heikes, Science **208**, 173 (1980).
[10] K. E. Heikes and F. H. Busse, Ann. N.Y. Acad. Sci. **357**, 28 (1980).
[11] K. Buhler and H. Oertel, J. Fluid Mech. **114**, 261 (1982).
[12] P. G. J. Lucas, J. M. Pfotenhauer, and R. J. Donnelly, J. Fluid Mech. **129**, 251 (1983).
[13] J. M. Pfotenhauer, P. G. J. Lucas, and R. J. Donnelly, J. Fluid Mech. **145**, 239 (1984).
[14] J. M. Pfotenhauer, J. J. Niemela, and R. J. Donnelly, J. Fluid Mech. **175**, 85 (1987).
[15] J. J. Niemela and R. J. Donnelly, Phys. Rev. Lett. **57**, 2524 (1986).
[16] F. Zhong, R. Ecke, and V. Steinberg, Physica D **51**, 596 (1991).
[17] F. Zhong and R. Ecke, Chaos **2**, 163 (1992).
[18] E. Bodenschatz, D. S. Cannell, J. R. de Bruyn, R. Ecke, Y. Hu, K. Lerman, and G. Ahlers, Physica D **61**, 77 (1992).
[19] Y. Tu and M. Cross, Phys. Rev. Lett. **69**, 2515 (1992).
[20] M. Fantz, R. Friedrich, M. Bestehorn, and H. Haken, Physica D **61**, 147 (1992).

[21] M. Neufeld, R. Friedrich, and H. Haken, Z. Phys. B **92**, 243 (1993).
[22] M. Cross, D. Meiron, and Y. Tu, Chaos **4**, 607 (1994).
[23] Y. Ponty, T. Passot, and P. Sulem (unpublished).
[24] J. Swift and P. Hohenberg, Phys. Rev. A **15**, 319 (1977).
[25] P. Hohenberg and J. Swift, Phys. Rev. A **46**, 4773 (1992).
[26] W. Pesch (private communication).
[27] Y. Hu, R. E. Ecke, and G. Ahlers, Phys. Rev. Lett. **74**, 5040 (1995).
[28] Y. Hu, R. E. Ecke, and G. Ahlers (unpublished).
[29] R. M. Clever and F. H. Busse, J. Fluid Mech. **65**, 625 (1974).
[30] F. H. Busse and R. M. Clever, J. Fluid Mech. **91**, 319 (1979).
[31] F. H. Busse, in *Hydrodynamic Instabilities and the Transition to Turbulence*, edited by H. Swinney and J. P. Gollub (Springer-Verlag, Berlin, 1981), p. 97.
[32] G. Ahlers, D. Cannell, and M. Dominquez-Lerma, Phys. Rev. Lett. **27**, 1225 (1983).
[33] A. Pocheau, V. Croquette, and P. Le Gal, Phys. Rev. Lett. **55**, 1094 (1985).
[34] M. S. Heutmaker, P. N. Fraenkel, and J. P. Gollub, Phys. Rev. Lett. **54**, 1369 (1985).
[35] G. Ahlers, D. S. Cannell, and V. Steinberg, Phys. Rev. Lett. **54**, 1373 (1985).
[36] M. S. Heutmaker and J. P. Gollub, Phys. Rev. A **35**, 242 (1987).
[37] V. Croquette, Contemp. Phys. **30**, 153 (1989).
[38] Y. Pomeau and P. Manneville, J. Phys. (Paris) Lett. **40**, L609 (1979).
[39] E. Siggia and A. Zippelius, Phys. Rev. Lett. **47**, 835 (1981).
[40] M. C. Cross, Phys. Rev. A **27**, 490 (1983).
[41] M. C. Cross and A. C. Newell, Physica D **10**, 299 (1984).
[42] H. Brand, in *Propagation in Systems far from Equilibrium*, edited by J.E. Wesfreid, H.R. Brand, P. Manneville, G. Albinet, and N. Boccara (Springer-Verlag, Berlin, 1988), p. 206.
[43] A. Pocheau, J. Phys. (Paris) **49**, 1127 (1989).
[44] A. C. Newell, T. Passot, and M. Souli, J. Fluid Mech. **220**, 187 (1990).
[45] A. C. Newell, T. Passot, and M. Souli, Eur. J. Mech. B **1**, 151 (1991).
[46] M. C. Cross and P. C. Hohenberg, Rev. Mod. Phys. **65**, 851 (1993).
[47] S. W. Morris, E. Bodenschatz, D. S. Cannell, and G. Ahlers, Phys. Rev. Lett. **71**, 2026 (1993).
[48] W. Decker, W. Pesch, and A. Weber, Phys. Rev. Lett. **73**, 648 (1994).
[49] R. Cakmur, B. Plapp, D. Egolf, and E. Bodenschatz (unpublished).
[50] Y. Hu, R. E. Ecke, and G. Ahlers, Phys. Rev. E **48**, 4399 (1993).
[51] Y. Hu, R. E. Ecke, and G. Ahlers, Phys. Rev. Lett. **72**, 2191 (1994).
[52] M. Assenheimer and V. Steinberg, Phys. Rev. Lett. **70**, 3888 (1993).
[53] Y. Hu, R. E. Ecke, and G. Ahlers, Phys. Rev. Lett. **74**, 391 (1995).
[54] Y. Hu, R. E. Ecke, and G. Ahlers, Phys. Rev. E **51**, 3263 (1995).
[55] M. Bestehorn, M. Fantz, R. Friedrich, and H. Haken, Phys. Lett. A **174**, 48 (1993).
[56] H.-W. Xi, J. D. Gunton, and J. Vinals, Phys. Rev. Lett. **71**, 2030 (1993).
[57] M. C. Cross and Y. Tu, Phys. Rev. Lett. **75**, 834 (1995).
[58] J. M. Rodríquez, C. Perez-Garcia, M. Bestehorn, M. Neufeld, and R. Friedrich, Phys. Rev. Lett. **74**, 530 (1995).
[59] F. Daviaud and A. Pocheau, Europhys. Lett. **9**, 675 (1989).
[60] A. Pocheau and F. Daviaud, Phys. Rev. E **54**, 353 (1996).
[61] S. W. Morris, E. Bodenschatz, D. S. Cannell, and G. Ahlers, Physica D **97**, 164 (1996).
[62] J. Liu and G. Ahlers, Phys. Rev. Lett. **77**, 3126 (1996).
[63] R. E. Ecke and Y. Hu, Physica A **239**, 174 (1997).
[64] Stability boundaries and SV angles were calculated using a computer code provided by Werner Pesch.
[65] H. Greenside and M. Cross, Phys. Rev. A **31**, 2492 (1985).
[66] P. Manneville, J. Phys. (Paris) **44**, 759 (1983).
[67] J. M. Rodríquez, C. Perez-Garcia, M. Bestehorn, M. Neufeld, and R. Friedrich, Chaos **4**, 369 (1994).
[68] J. R. de Bruyn, E. Bodenschatz, S. W. Morris, S. Trainoff, Y. Hu, D. S. Cannell, and G. Ahlers, Rev. Sci. Instrum. **67**, 2043 (1996).
[69] The cell and the CO_2 gas pressure are the same as for Refs. [53] and [54]. The slightly different fluid properties in this paper are based on updated CO_2 data given in Ref. [68].
[70] This cell had $d=1.031\pm0.005$ mm and gave $\Delta T_c=1.51\pm0.01$ °C.
[71] C. W. Meyer, G. Ahlers, and D. S. Cannell, Phys. Rev. Lett. **59**, 1577 (1987).
[72] C. W. Meyer, G. Ahlers, and D. S. Cannell, Phys. Rev. A **44**, 2514 (1991).
[73] F. H. Busse, Rep. Prog. Phys. **41**, 1926 (1978).
[74] E. Bodenschatz, J. R. de Bruyn, G. Ahlers, and D. S. Cannell, Phys. Rev. Lett. **67**, 3078 (1991).
[75] Y. Hu, L. Ning, and R. E. Ecke (unpublished).
[76] Y. Hu, Ph.D. thesis, University of California, Santa Barbara, 1995.
[77] F. Zhong, R. Ecke, and V. Steinberg, J. Fluid Mech. **249**, 135 (1993).
[78] R. E. Ecke, Y. Hu, R. Mainieri, and G. Ahlers, Science **269**, 1704 (1995).
[79] The first calculation was reported by G. Küppers in Ref. [3]. The value quoted in this paper for our particular Prandtl number is from T. Clune and E. Knobloch (private communications).
[80] Y. Hu, R. E. Ecke, and G. Ahlers (unpublished).
[81] V. Croquette, Contemp. Phys. **30**, 113 (1989).
[82] V. Steinberg, G. Ahlers, and D. S. Cannell, Phy. Scr. **32**, 534 (1985).
[83] J. M. Rodríguez, M. Bestehorn, C. Pérez-García, R. Friedrich, and M. Neufeld, Phys. Rev. Lett. **74**, 530 (1995).
[84] M. Assenheimer and V. Steinberg, Nature **367**, 345 (1994).